Project Number: ERT _ MQP _ 12Q2

MODELING OF CARGO TRANSPORT VIA MOLECULAR MOTORS

Major Qualifying Project Report completed in partial fulfillment
of the Bachelor of Science degree at
Worcester Polytechnic Institute

Andrew O'Neill

March 12, 2013

Professor Erkan Tüzel, Advisor
Department of Physics

Abstract

The motor protein kinesin-1 plays an essential role in transporting cellular cargoes within eukaryotic cells. When bound to a microtubule in the presence of ATP, kinesin-1 motors repeatedly take steps along the microtubule's protofilaments. A group of kinesins "walking" together can cooperatively transport various cellular cargo over relatively long distances. While much is known about the transport by individual kinesin-1 molecules, very little is known about the specific mechanisms of cooperative kinesin-based transport. Here, we developed a two-dimensional stochastic model of cargo transport via multiple kinesins and compared our simulation results with experimental data. The simulation focuses on the modeling of quantum dot cargoes transported along a microtubule. We found that high motor densities lead to increased run lengths, increased association times and decreased velocities, and that our stochastic model recapitulates experimental data reasonably well.

Contents

List of Figures

List of Tables

Chapter 1

Introduction

1.1 Transport in cells

Cells, the fundamental building blocks of life, are large collections of organelles held together by a plasma membrane. These organelles, such as the mitochondria, Golgi apparatus, and the nucleus found in eukaryotic cells, exist to carry out specific, vital functions within the cell. Also contained within the plasma membrane is the cytoskeleton, a protein scaffold that gives the cell structures and plays a large role in intracellular transport and cell division [14]. Figure 1.1 shows a typical cellular structure for an animal cell.

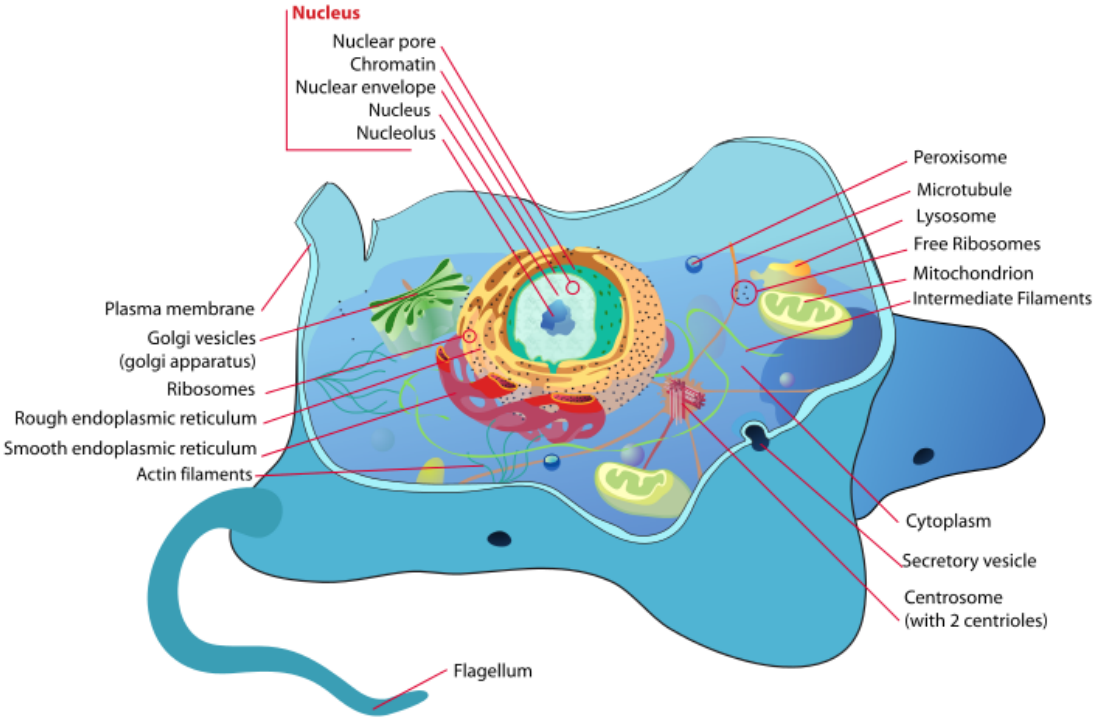

Figure 1.1: A cartoon revealing some of the various organelles that can be found inside eukaryotic animal cells. Image by Ruiz [16].

Some prokaryotic cells, like bacteria, rely on diffusion for intracellular transport. The relatively small size of a bacterium allows for efficient transport of waste products and nutrients across the cell plasma membrane via diffusion. To demonstrate, consider the bacteria *E. coli*, which typically has a diameter of $0.5\,\mu$m and a length of $2\,\mu$m [15]. With a diffusion constant $D \simeq 10^3\,\mu\text{m}^2/\text{s}$ [2], we can calculate the average time it would take for a small particle to diffuse across the length of the cell to be $t \simeq 20\,\text{ms}$. By comparison, for a eukaryotic cell with a length of $50\,\mu$m, the same particle would take $1.25\,\text{s}$ to diffuse across the entire cell. This shows that intracellular diffusion is ineffective over longer distances and with bigger cargos, so larger cells require a more efficient transportation system.

Unlike bacteria, neuron cells in animals rely on a microtubule-based transport system to distribute resources within the cell, and to send communications quickly through complex neural networks. Within the cytoskeleton is a network of microtubules (MTs), along which cellular cargo can be transported. Small motor proteins like dynein and kinesin walk along MT protofilaments and carry neuronal cargoes to different parts of the cell at great speeds. Huntington's disease and other disorders are caused by defects in MT-based transport that lead to accelerated decay rates of neurons [11].

Another important example of MT-based transport can be observed during cell division, in which mitotic spindles are assembled by various motor proteins and organized into two opposite polar sets. This bipolar organization is crucial in the separation of daughter chromosomes during mitosis. Hundreds of Eg5 kinesin-5 motor proteins bind to two antiparallel MTs and step along each to create a driving force that helps separate the two sets of chromosomes [3].

1.2 Microtubules

An important part of the cytoskeleton, MT networks provide the cell structure and a means of intracellular transport. MTs typically emerge from a cell's MT organizing center (MTOC) and branch out into the cell. Motor proteins like dynein and kinesin can bind and walk along individual MTs, allowing for transport of cellular cargoes to different parts of the cell. Other proteins, like the MT-severing protein katanin, help regulate MT properties like polymerization and depolymerization rates [12].

MTs are made up of α- and β-tubulin dimer subunits. These dimers are polymerized end-to-end into chains known as protofilaments. A typical MT is essentially a hollow cylinder composed of 13 associated protofilaments. Because they are made up of $\alpha\beta$ heterodimers, the MT also has a distinct polarity: the (-) end has β-tubulin exposed and the (+) end has α-tubulin exposed. The cell's MTOC stabilizes a MT's minus-end, while the plus-end is susceptible to dynamic instability, a term describing the polymerization and depolymerization of the MT from its plus-end [14].

The unique $\alpha\beta$-tubulin dimer protofilaments can also serve as tracks along which motor proteins may transport cargo [14]. Because of the polarity and structure of MTs, different classes of molecular motors can travel in different manners and directions, making MT-based transport useful for a variety of tasks.

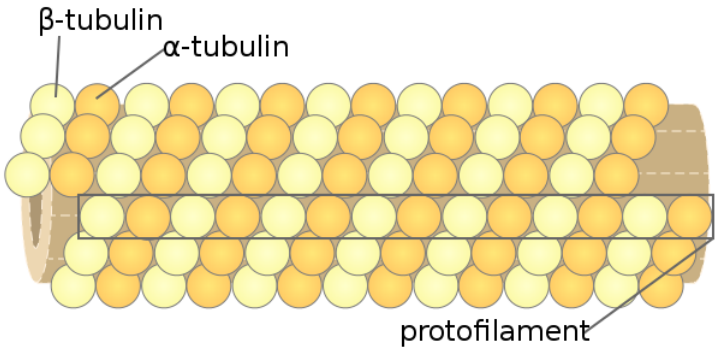

Figure 1.2: A cartoon depiction of a MT's structure and assembly. Thirteen protofilaments bound together make up the MT. The polarity of the $\alpha\beta$ dimers determines which end of the MT is the (+) end and which is the (-) end. Image by Zlir'a [20].

1.3 Kinesin-1 molecular motors

Motor proteins are an essential part of MT-based transport. As the name suggests, molecular motors move along MT protofilaments and have the ability to carry cellular cargos with them. These proteins can be broken into two distinct families: dynein and kinesin motors. Dyneins are complex, minus-end directed motors that assist in MT movement in flagella and cilia, as well as organelle and vesicle transport. Kinesin motors are structurally simpler proteins that assist in cell division and the transport of cellular cargo [6].

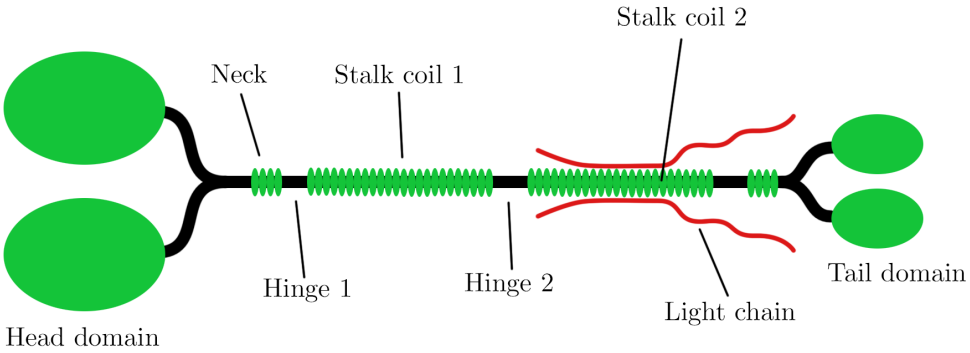

Figure 1.3: A depiction of kinesin-1's chemical structure. The head domain steps along a MT protofilament, while the tail domain can bind to cellular cargo.

While motor structure varies within the kinesin family, the motor kinesin-1 shares many structural characteristics with other kinesins. Kinesin-1 is a protein dimer composed of two heavy chains bound to two light chains (see Figure 1.3.) The protein consists of three distinct sets of domains: the two tail domains, the stalk, and the two head domains. The tail domain includes the pair of light chains and is used to bind to cellular cargo. Kinesin-1's stalk domain is a coiled-coil domain that provides structure to the motor. The motor's head domain is made from heavy chains and allows the motor to bind to and walk along MT protofilaments [6].

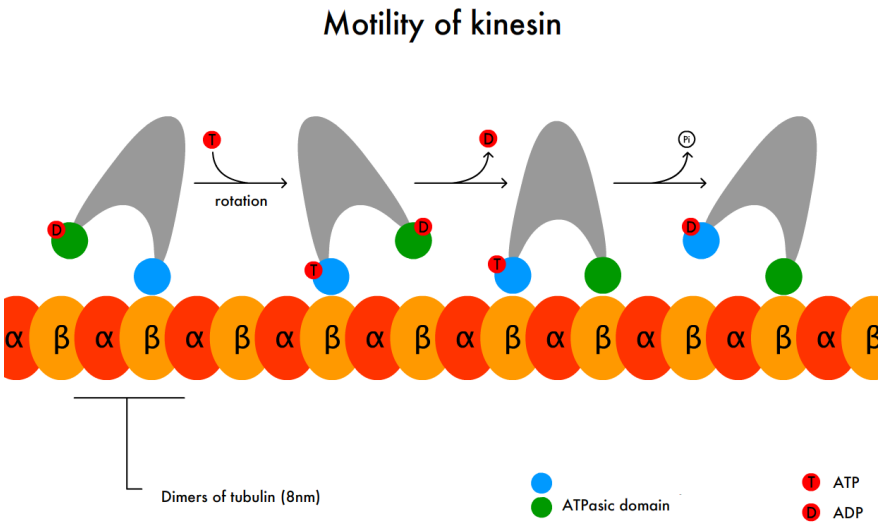

Figure 1.4: Kinesin-1's stepping cycle. In the presence of ATP, kinesin experiences a conformational change that results in a single 'step' forward. As this process repeats itself, the motor's cargo is transported along the MT. Image by Slagt [18].

All motor proteins use ATP hydrolysis to convert chemical energy to mechanical work, usually in the form of walking or sliding along a MT. Each of kinesin-1's two head domains has one binding site for ATP and another for the MT. ATP hydrolysis causes a conformation change between the head domain and the stalk, resulting in head movement (Figure 1.4) [6]. Kinesin's head domains take turns stepping towards the MT's minus-end and the tail domains pull any bound cargo along for the ride. This biochemical process can be approximated by the following reaction:

$$K + ATP \xrightarrow{k_a} K \cdot ATP \xrightarrow{k_b} K + ADP \tag{1.1}$$

where k_a and k_b are reaction rate constants [17]. Kinesin-1's stepping process can be described as follows (shown in Figure 1.4:)

1. Kinesin's unbound head domain diffuses toward the next available binding site.
2. An ATP molecule binds to the head domain that is diffusing forward, thus locking it onto the binding site. This process occurs with a binding rate k_a.
3. The trailing head domain detaches from its binding site by converting its ATP molecule to ADP. This process occurs with a binding rate k_b.
4. Kinesin's newly unbound head diffuses forward to the next binding site. This stepping process continues as long as the motor is bound to a protofilament.

This step cycle depends on the concentration of ATP available to the motor. The step size for a kinesin-1 motor is 8 nm, so we can calculate the motor's velocity v as a function of ATP concentration c:

$$v(c) = \frac{d}{k_b^{-1} + (k_a c)^{-1}} \,, \tag{1.2}$$

as shown by Schnitzer et al. [17].

Single molecule experiments provide evidence for kinesin's "hand-over-hand" stepping. Because of the 8 nm length of a tubulin-dimer, kinesin motors take 8 nm steps as they travel along the MT. Single kinesin molecules have been shown to exert pulling forces of up to 5 pN during cargo transport. Considering kinesin's mechanical work and the energy available from ATP hydrolysis, the efficiency of a single kinesin molecule's step cycle is around 50% [6].

There are many aspects of kinesin based transport, particularly under crowded conditions, that remain a mystery to researchers in the field. Computational models done in conjunction with experiments are our best hope to fill this knowledge gap and understand the complex interactions that occur during these processes.

1.4 Models of transport

Considering the mechanics and experimental data available on kinesin transport, various research groups have attempted to model kinesin dynamics using computer simulations with varying degrees of success. In the following section, we will discuss some of these models.

1.4.1 Lattice model

Perhaps the simplest model is the one-dimensional lattice model, such as the one implemented by Leduc et al. [10]. In this model, the MT is represented as a single, one-dimensional lattice with N motor binding sites. The motor proteins are then modeled as simple particles that can bind to sites on the lattice. Using discrete time steps, the simulation chooses random binding sites and applies the following rules:

1. If a site is empty, a new motor attempts to occupy that site with a probability k_{on} (proportional to the concentration of motors in the solution.)

2. If a site is occupied, the motor leaves the lattice with the probability k_{off}. If the motor remains attached and the next site is unoccupied, it moves to that site.

Under these rules, motors are constantly associating, dissociating and stepping along the MT. This type of lattice model is good for modeling small groups of motors without cargo, but unfortunately doesn't include calculations about forces or other motor dynamics.

1.4.2 Transition rate model

The Transition Rate (TR) model is a motor-based transport model introduced Klumpp and Lipowsky [7]. The state-based model considers a cellular cargo being transported by fixed number of motor proteins. These motors are permanently bound to the cargo, but may bind

and unbind from the MT with effective binding and unbinding rates. Rather than modeling the specific mechanics, the TR model uses probabilistic states to calculate properties like run length, run duration, cargo velocity, average number of bound motors, etc. The TR model operates on the cargo state-driven equation

$$\varepsilon_{n+1}P_{n+1} = \pi_n P_n \ , \tag{1.3}$$

where for the state $|n\rangle$, in which n motors are bound to both the cargo and the MT, P_n is the probability the cargo is in state $|n\rangle$, ε_n is the unbinding rate of the a single motor and π_n is the binding rate of a single motor. This equation simply shows how the opposing binding and unbinding rates probabilistically change the state $|n\rangle$, ε_n. Using this, a general expression is calculated as

$$\langle \Delta x_b \rangle = \frac{v_1}{\varepsilon_1}\left[1 + \sum_{n=1}^{N-1}\prod_{i=1}^{n}\frac{v_{i+1}\pi_i}{v_i\varepsilon_{i+1}}\right] \ , \tag{1.4}$$

where N is the total number of motors bound to the cargo, n is the number of motors bound to both the cargo and the MT, and v_n is the cargo velocity with n bound motors [7]. While this model provides a simplified view of kinesin transport, it neglects some of the more complicated mechanical interactions in the system.

1.4.3 Mechanistic model

A more realistic model of cargo transport has been developed by Korn et al. [9]. The mechanicistic cargo transport (MCT) model (illustrated in Figure 1.5) uses a Langevin equation approach that can calculate the two-dimensional position of a circular cargo as a function of time. In the model, the cargo is covered with N_{tot} evenly distributed, permanently bound kinesin motors. When bound to the MT, these motors take 8 nm steps with a foward stepping rate λ_s^0 and act as a spring that can apply forces and torques to the cargo. The motors also experience a force-dependent escape rate ε

$$\varepsilon = \varepsilon_0 \exp(F_m/F_d) \ , \tag{1.5}$$

where F_m is the force felt by the motor, ε_0 is the unstressed escape rate, and F_d is the kinesin detachment force [9]. Similarly, the kinesin motors are also modeled with a force-dependent velocity

$$v_m = v_0\left(1 - \frac{F_m}{F_s}\right), \ \ 0 < F_m < F_s \ , \tag{1.6}$$

with the unstressed velocity v_0 and the stall force F_s.

An important difference between this mechanistic approach and the previous models is the inclusion of detailed physical interactions between the cargo, kinesins and MT. For example, as the circular cargo rotates and moves in the model, bound motors may experience relatively large forces and unbind from the MT, while new motors may intersect and bind to the MT [9]. The computer simulations associated with this type of model may be significantly more computationally expensive than the lattice or TR models, but they also include more realistic mechanics.

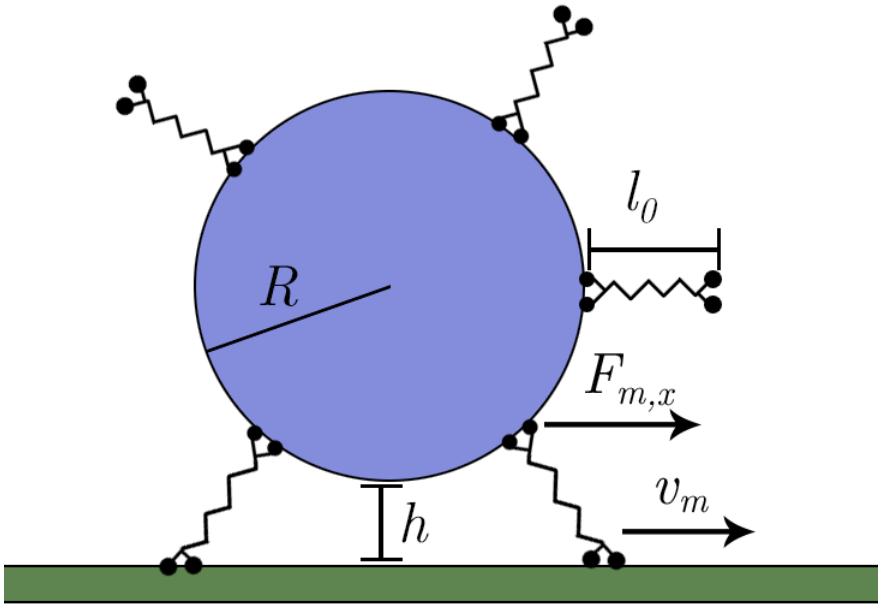

Figure 1.5: A cartoon representation of the MCT model. N_{tot} motors are uniformly distributed onto the cargo, and any motors that intersect the MT can bind to it. Motors bound to the MT take 8 nm steps along it, transporting the cargo along the MT until they disassociate.

Chapter 2

Experiments and modeling

2.1 Bead assay experiments under crowded conditions

Relatively little work has been done involving kinesin-1 motility at higher motor concentrations [4]. Instead, much of the current experimentation and modeling in the field has been focused on understanding motility at lower densities, where it is often easier to interpret experimental results. Kinesin crowding may involve more intricate dynamics that do not apply to lower density situations, like motor entanglement, step synchronization, or multi-protofilament transport.

The Ross lab at the University of Massachusetts-Amherst have recently performed *in vitro* bead assay experiments with kinesin-1 under crowded conditions in order to shed some light on these systems. In these experiments, they track streptavidin-coated quantum dots as they are carried by kinesin-1 motor proteins along MTs. These motors are allowed to associate and dissociate from the MT, just as they would *in vivo*. It was found that increasing the motor concentration led to increased quantum dot association times, larger run lengths before dissociating, and reduced transport velocities. This kinesin-1 density increase also created distinct pauses during transport [4]. During these pauses, shown in Figure 2.1 the cargo would not move for long periods of time, usually on the order of seconds.

The Ross lab also analyzed tracking data from single GFP-labeled kinesin-1 motors in similar conditions. Individual kinesins showed similar behavior to the quantum dots, with the exception that single kinesin tend to dissociate from the MT much more quickly. The results suggest that the discrete pauses observed in both sets of experiments may be caused by obstacles located on the MT's surface: the motors are forced to wait until the obstacle unbinds to proceed [4]. These results provide valuable insight into the complex interactions that occur during kinesin-1 transport.

Another study done by [19] observed Kip3p motors at high densities on MTs. Kip3p is a member of the kinesin-8 family, a group of motors known for being extremely processive. Unlike kinesin-1, Kip3p specializes in MT depolymerization rather than cargo transport. The researchers found that Kip3p's off-rate at the end of the MT was dependent on the concentration of Kip3p motors nearby. This effect was observed even when the MT's plus ends were stabilized, effectively eliminating any chance of depolymerization. Kinesin-1 motors were also found to have density dependent end off-rates but curiously, this effect was

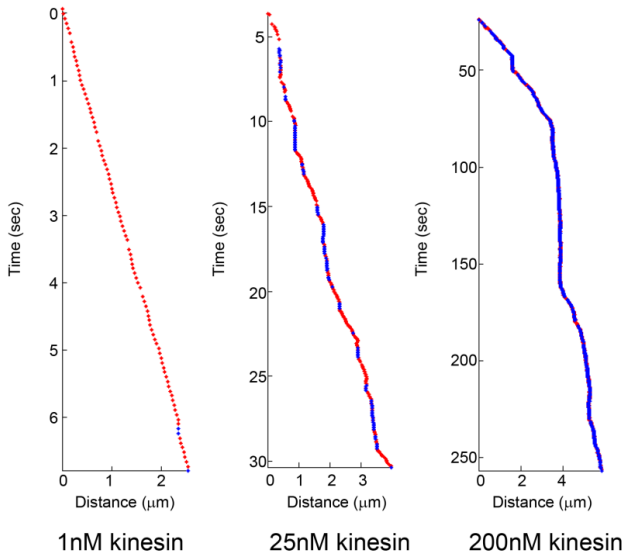

Figure 2.1: Sample kymographs at different kinesin concentrations [4]. As the motor density increases, pauses in the quantum dot's movement become more frequent.

not observed with a mix of Kip3p and kinesin-1 [19]. While the exact cause of this off rate dependence is unknown, these types of experiments offer new ideas about motor interactions at high concentrations and allow for direct comparison with existing motility models.

Unfortunately, many of the current kinesin transport models have been oversimplified and may not apply to the higher density situations that have been observed. Regardless of motor concentration however, the presence of obstacles on the MT plays a large role in cargo transport. Most transport models ignore the important cases where motors are physically blocked by stationary obstacles. It is likely that these sorts of obstacles are the primary cause of cargo pauses during kinesin transport; if a MT's protofilaments are blocked, the motors cannot proceed until the way is cleared.

The obvious question is: what are these "obstacles" that block protofilaments? They could be caused by a number of things: protofilament defects, defective motors, or anything else that is able to bind to MTs. In the case of motor crowding during transport, it is conceivable that some number of kinesin are defective or 'dead' motors. Here dead motors simply mean damaged motors, ie. due to purification, that may bind to MTs as other motors do, but cannot step, effectively creating a temporary roadblock [5]. Dead motors will eventually dissociate from the MT, allowing the paused motors to proceed again. Unfortunately, little is known about these dead motors and their effects on cargo transport.

The potential presence of dead motors and other protofilament obstacles appear to play a very important role in kinesin-based transport, and should not be overlooked in transport models. Models that incorporate factors like dead motors, as well as properties of the imaging system are necessary to develop a better understanding of these systems. In the next section, we will explain how to take into account effects of the imaging sysstem into the simulations.

2.2 Model convolution microscopy

In order to make accurate assessments between experiments and models, the data must be presented and analyzed in a similar fashion. Model Convolution Microscopy (MCM) is a practice in which simulation data is post-processed to emulate a microscope system [13]. Regrettably, many models omit this exercise, permitting researchers to unfairly compare grainy experimental data with extremely precise theoretical predictions.

The first step in the MCM process is to create a two-dimensional contour image that will represent a component of the system. This contour usually corresponds to the object being tracked under the microscope. Next, the contour is placed on a grid and its interior is filled within the grid. Grid cells with contour segments inside them may be included, provided a large enough fraction of the cell is within the contour bounds (Fig. 2.2) [13].

After discretizing the contour, the Point Spread Function (PSF) is obtained either experimentally or theoretically. When obtained experimentally, the resulting PSF naturally includes microscope lens abnormalities and other optical effects, but is constrained to the same resolution used in the imaging system. However, a theoretical PSF can use any resolution. Here is an example of a theoretical PSF using the Airy function

$$I = \left| \frac{2J_1(\rho)^2}{\rho} \right| \tag{2.1}$$

where

$$\rho = \frac{2\pi NA}{\lambda} r \ , \tag{2.2}$$

λ is the wavelength of light, r is the radial distance from the origin and NA is the numerical aperture [13]. Figure 2.2B shows a plot of the PSF as a function of the radial distance.

The next step in the process is the actual convolution of the image. This process projects the light intensity of each pixel in the image onto its neighbors. These intensities are summed over all of the pixels, giving the resulting image a blurred effect (Fig. 2.2) [13]. Finally, the image's mean and standard deviation signal are fitted to the experimental images. In order to gather noise data, background portions of the experimental images are analyzed. Using the background's standard deviation, Gaussian noise is applied to the convolved image to complete the process [13].

MCM is a powerful method that allows simulation and experimental data to be compared more fairly. While few modern models use this technique, the model we have developed for the subject of this paper does indeed utilize it. This simulation model aims to improve on the weaknesses of current models and shed some light onto the complex dynamics that occur during crowded kinesin-1 transport.

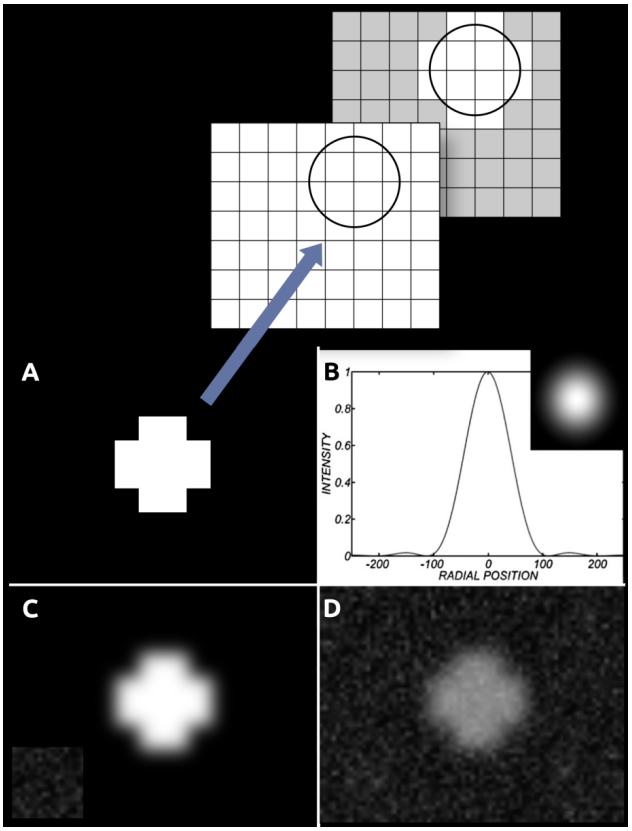

Figure 2.2: A simple overview of the MCM process. (A) A predefined shape (in this case, a circle) is discretized into individual pixels. (B) An example Point Spread Function (PSF) of light as a function of the readial distance r. (C) The discretized shape from A is convolved using the PSF. Each pixel's light intensity is projected onto its neighbors and summed. (D) The convolved image is matched to the experimental image and noise is added accordingly. Figure adapted from Nguyen et al. [13].

2.3 The model

In order to explain the distinct pauses and observed run lengths in high-density kinesin-1 based transport, we developed a two-dimensional stochastic model. We found that existing models worked well for relatively low kinesin motor concentrations, but failed to accurately describe transport at higher concentrations. The model introduced here attempts to improve these shortcomings, while introducing the use of MCM to allow more accurate comparisons with experimental data. Our simulation is written using the Fortran programming language and it uses discrete time intervals to update the system as it evolves.

Our model is most closely related to the MCT model described in Section 1.4.3. It features a circular cargo placed on a MT with randomly distributed kinesin motors on the surface. As a motor's tail domain intersects the cargo, the motor binds to the cargo and applies a force and torque as it steps along the MT. One of the primary differences between this and the MCT model is that our model features motors distributed along the MT and does not assume motors are permanently bound to the cargo. As the simulation progresses,

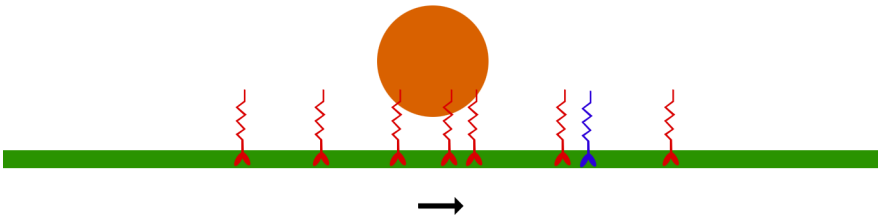

Figure 2.3: A cartoon depiction of the cargo-assay model. Regular motors (seen in red) carry the quantum-dot cargo along the MT. Dead motors (blue) cannot step, and can cause traffic jams along the MT until they stochastically unbind. We believe that these dead motors are the primary cause of pausing in crowded kinesin-1 motility assays.

motors bind and unbind to the cargo until it dissociates and the simulation ends.

2.3.1 Kinesin-1 motor dynamics

In our model, each molecular motor is modeled as a pseudo-spring of rest length l_0. If a motor is stretched, it exerts a restoring force; however, it has been shown that kinesin-1 may be modeled as a simple flexible polymer that exerts little or no restoring force when compressed [9]. Thus, we chose to express our motors' spring force as

$$F_m = \begin{cases} -\Delta l\, k, & \text{if } \Delta l > 0 \\ 0, & \text{if } \Delta l < 0 \end{cases} , \tag{2.3}$$

where Δl is the compression/extention distance and k is the motor's spring constant.

Similar to the MCT model, our model features a force dependent motor unbinding rate k_{off} [9]

$$k_{\text{off}} = k_{\text{off},0}\, \exp(F_m/F_d) , \tag{2.4}$$

where F_m is the force felt by the motor, $k_{\text{off},0}$ is the unstressed escape rate, and F_d is the kinesin detachment force. This equation essentially means that motors under stress are more likely to stochastically unbind than unstressed motors. This is particularly significant as the cargo experiences Brownian motion that can cause bound motors to unbind very quickly.

Similarly, kinesin-1 have also been shown to have a force-dependent velocity . The motors in our model stochasticly take the typical 8 nm steps along the MT with a stepping rate λ_s, resulting in an average velocitiy v_m that varies with the motor force F_m [6]. Our model uses a linear force-velocity relationship given by

$$v_m = v_0 \left(1 - \frac{F_m}{F_s}\right) , \quad 0 < F_m < F_s , \tag{2.5}$$

with the unloaded velocity v_0 and the stall force F_s. As a motor experiences a positive force, it's stepping rate λ_s decreases linearly. Shown in Fig 2.4, a motor under a large enough load

will "stall" and stop stepping completely. Motors under no load will step at the unloaded stepping rate λ_s^0 [9].

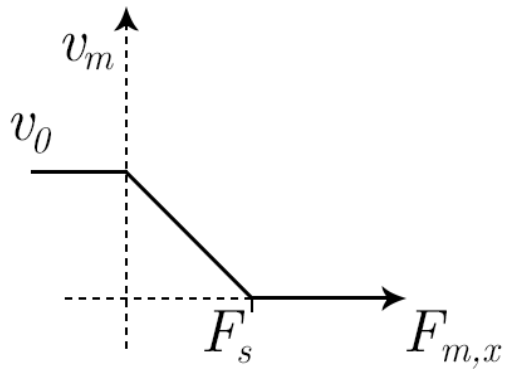

Figure 2.4: Plot of the force-velocity relationship of a single motor in our model (Eq. 2.5.) Motors experiencing a positive force F_m greater than or equal to the stall force F_s cannot step along the MT.

Our model defines ψ as the concentration of motors on the MT in a given simulation. We choose the values of ψ such that they correspond to the concentrations used in experiments. In order to understand the meaning of these values, we can roughly express ψ in terms of MT length, as shown in Figure 2.5 [4]. For example, this relationship shows that the motor concentration $\psi = 100\,\text{nM}$ kinesin equivalent to $15.215\,\text{motors}/\mu\text{m}$ of a single MT protofilament.

One important difference between our model and the previous models is the inclusion of dead motors [7, 9, 10]. We define the ratio of dead motors by ρ. These motors cannot step, but are otherwise treated as the other motors. Regular motors cannot step forward until the binding site in front of them is cleared. A binding site occupied by a dead motor will only free up once the dead motor stochastically unbinds.

2.3.2 Cargo dynamics

The cargo being transported in the model is represented by a simple circle of radius r that is subject to the forces and torques exerted by the motors carrying it. In each time step of the simulation, the program checks for new intersections between the motors and cargo. If a motor on the MT intersects the cargo, this motor is considered bound to the cargo and its tail domain is then fixed to the edge of the cargo nearest to its intersection point. Conversely, motors bound to the cargo that stochastically unbind remain on the MT, where they may rebind to the cargo.

Cargo movement is influenced by external forces acting on it. In the stokes limit, acceleration is negligible. One can therefore write the net force on the cargo as

$$F_{tot} = ma \approx 0\ . \tag{2.6}$$

In the absence of inertia, forces on the cargo due to motors and thermal fluctuations are

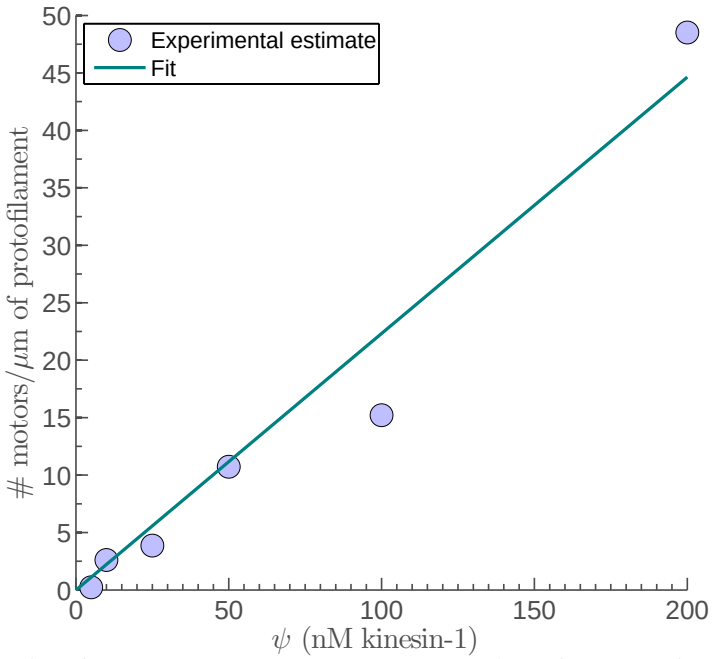

Figure 2.5: The relationship between motor concentration ψ and motor density per protofilament from experimental estimates.

balanced by friction forces, shown by

$$0 = \sum_{i=1}^{n_b} F_{m,i} + F_B - F_F \ , \tag{2.7}$$

where the frictional force F_B can be rewritten as

$$\zeta v = \sum_{i=1}^{n_b} F_{m,i} + F_B \ . \tag{2.8}$$

The Gaussian distributed Brownian force F_B can be described by the following expressions for average random force $\langle F_B \rangle$ and the variance of the force $\langle F_B^2 \rangle$

$$\langle F_{B,\alpha} \rangle = 0 \tag{2.9}$$

$$\langle F_{B,\alpha}^2 \rangle = 2D\Delta t \ , \tag{2.10}$$

where $\alpha = x, y, z$ and the diffusion coefficient D is defined as

$$D = \frac{k_B T}{\zeta} \ , \tag{2.11}$$

with the Boltzmann constant k_B, the temperature of the medium T and the friction coefficient ζ. In the model, Eqs. 2.9 and 2.10 are used to generate random forces on the cargo. With these equations, we can write the velocity of the cargo as

$$\frac{dr}{dt} = v = \frac{\sum_{i=1}^{n_b} F_{m,i} + F_B}{\zeta} \ . \tag{2.12}$$

Using this relation, we can calculate the cargo's position by Euler integration.

2.3.3 Model visualization

In order to visualize the events occuring in our model, we designed our simulations to periodically create raw OpenDX graphics files [1]. These files include position, orientation and shape data for all simulation objects and are later processed into individual movie frames (see Fig. 2.6 for an example.) To visualize motor forces, the DX files are configured to vary a motor's color with the force experienced by it. Similarly, dead motors are rendered as white. This process allows us to visualize some of the complex interactions that occur in the simulation and also to verify that the model is working properly.

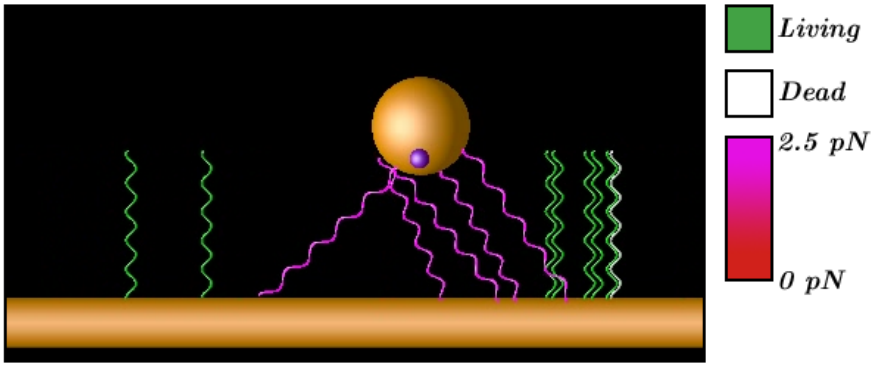

Figure 2.6: A single video frame from a DX visualized cargo-assay simulations [1].

The second visualization method used in our simulations is the MCM process described in Section 2.2 [13]. The cargo's position is periodically written to a file and processed into individual movie frames (see Fig. 2.7 for an example.) The point of this visualization process is to directly simulate experimental data, so that the model and experiment can be fairly compared.

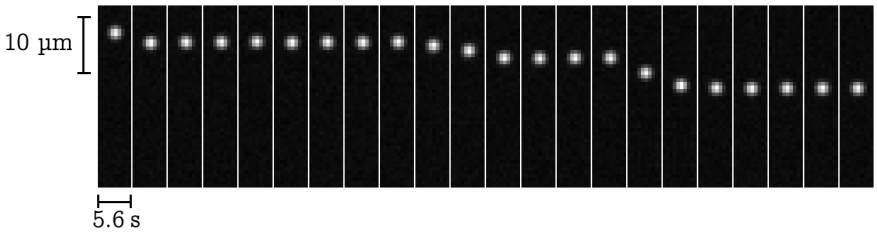

Figure 2.7: A sample montage from a cargo-assay simulation run using the MCM technique. This process allows simulation data to mimic the properties of the imaging system into the simulation data, allowing direct comparison with experimental results. Each frame in the montage represents 5.6 seconds of simulation time.

2.3.4 Model psuedocode

Below is the psuedocode outline of the our simulation. The simulation was written in the Fortran programming language. The random number generator algorithm is a variant of the Subtractive Method algorithm from Knuth [8].

Model Initialization: Run once at the beginning of each simulation

1. Calculate the total number of motors in the simulation N in accordance with the desired motor concentration.

2. Place the first motor directly beneath the cargo and initiate binding.

3. Randomly place the remaining $N-1$ motors on the MT. Mark some percentage of the motors as dead motors in accordance with the dead motor percentage ρ.

Main Loop: Run every time step until the simulation ends

1. Check all motors for tail domain intersections with the cargo. If an intersection is found, move its tail position to the edge of the cargo and mark it as "bound."

2. Calculate the spring forces of each bound motor and the random Brownian forces on the cargo.

3. Update the cargo's position and rotation due to these forces. Update the tail positions of any bound motors accordingly.

4. Loop over all motors and determine if they will stochastically unbind from the MT. Unbound motors are randomly placed elsewhere on the MT to keep the motor concentration constant.

5. Loop over all non-dead motors and determine if they will step. A step is automatically rejected if the binding site in front of the motor is filled.

6. Write motor and cargo data to external files. Convolution and/or OpenDX data writing also occurs at this step.

7. End the simulation if no motors are bound to the cargo.

8. Increment the time t by Δt.

2.3.5 Summary

In this chapter, we examined the experimental findings of kinesin transport at high concentrations. Various models of kinesin-1 transport were explored and analyzed. We developed a model that builds upon the weaknesses of prior models and can simulate kinesin transport at high concentrations using mechanistic modeling and MCM processing to emulate experimental results.

Chapter 3

Results

In the following sections, we outline three variants of our stochastic transport simulations: the Mechanistic Cargo Transport (MCT) model, single motor (SM) model, and Improved Mechanistic Cargo Transport (IMCT) model. The MCT model is compared with model data from Korn et al. [9], while the single motor and IMCT models' results are compared with experimental data from Conway et al. [4].

3.1 Analysis of simulation data

In this section we briefly discuss the terminology used in the simulations and the techniques used to obtain them. In all three models presented in this paper, the simulation continues indefinitely until the cargo (or GFP-labeled motor, in the case of the SM model) dissociates from the MT. We refer to the net x-distance traveled by the cargo during the simulation as the run length Δx_b. The net time from beginning of the simulation start to cargo dissociation is refered to as the association time Δt_b. Using these two values, we can also calculate the mean run velocity $\langle v_b \rangle$. During the simulation, we record the number of MT- and cargo-bound motors n_b for each timestep.

In addition, the IMCT simulations use a model convolution subroutine to emulate experimental results. These convolution movie frames are processed with a MATLAB script by collaborator Derek Woods of the Ross lab. This script analyzes cargo movement and determines when and for how long pauses in transport occur.

3.2 Mechanistic cargo transport simulation results

The MCT simulations in general produced persistent and fast cargo transport with hundreds of motors permanently bound to the cargo (parameters shown in Table 3.1. Figure 3.1 illustrates this concept very clearly. The number of permanently bound motors varies from 120 to 440. The results show that the run length increases roughly exponentially with the total number of motors bound to the cargo N_{tot}.

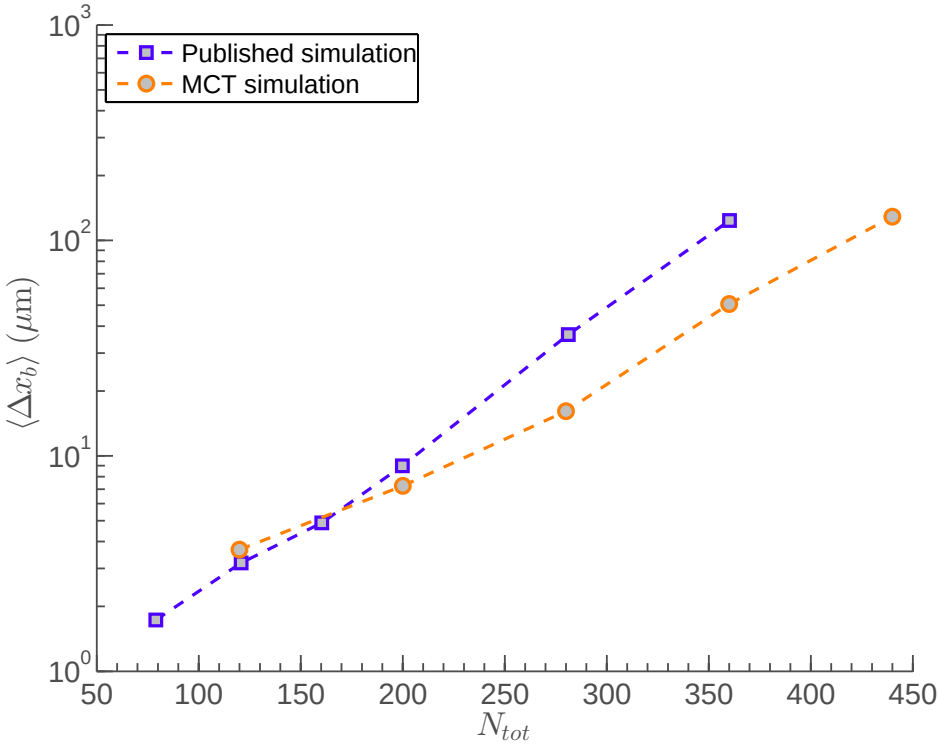

Figure 3.1: Measured relationship between the mean cargo run length and total motors bound to cargo N_{tot} for the MCT simulations we preformed and published data. The purple data points show the original MCT simulation results and the orange data points show our implementation of model [9].

Figure 3.2 exhibits a similar behavior with the cargo's association time. The lowest number of bound motors $N_{tot} = 120$ yields a association time of 6 seconds, while $N_{tot} = 440$ stays bound for almost 700 seconds.

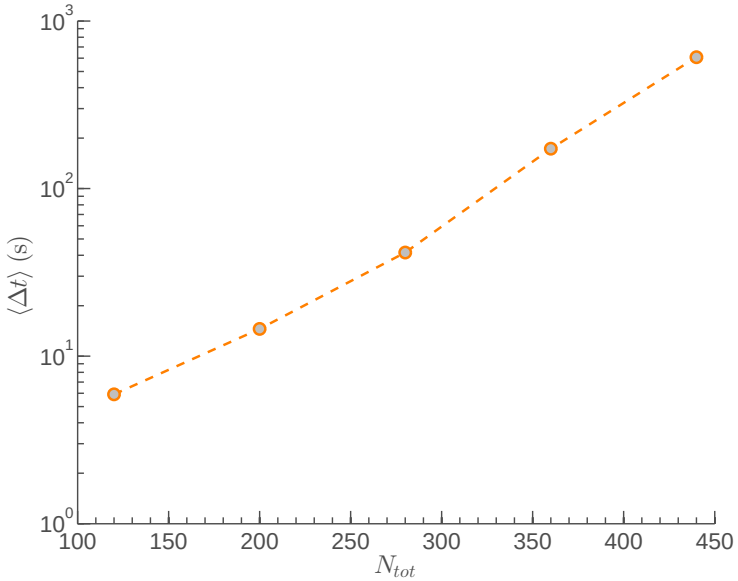

Figure 3.2: Measured relationship between the mean cargo association time and total motors bound to cargo N_{tot} for the MCT simulations.

Parameter	Typical Value	Meaning
R	$1\,\mu$m	Cargo radius
T	$293\,$K	Ambient temperature
η	$1, \ldots, \mathbf{7.6}, \ldots, 100\,$mPa s	Viscosity
h	$\mathbf{4}, \ldots, 14\,$nm	Height from cargo bottom to MT
$k_{off,0}$	$1\,\mathrm{s}^{-1}$	Unstressed escape rate
π_{ad}	$5\,\mathrm{s}^{-1}$	Binding rate
N_{tot}	$120, \ldots, 440\,$motors	Motors bound to cargo
F_d	$3\,$pN	Detachment force
k	$10^{-5}, \ldots, \mathbf{10^{-4}}, \ldots, 10^{-3}\,$N/m	Kinesin spring constant
δ	$8\,$nm	Kinesin step size
v_0	$1\,\mu$m/s	Maximum motor velocity
$\lambda_s^0 := v_0/\delta$	$125\,\mathrm{s}^{-1}$	Forward stepping rate
F_s	$5, \ldots, \mathbf{6}, \ldots, 8\,$pN	Stall force
l_0	$65\,$nm	Unstressed motor length
Δt	$1\,\mu$s	Simulation time step

Table 3.1: Simulation parameters used in the MCT model. If a range is given, the value in bold was the one used in the simulations unless otherwise specified. All parameters taken from [9].

It is important to note that, our MCT implementation features a consistent decrease in cargo velocity as the number of bound motors increases. These results, shown in Figure 3.3, differ from velocities of the original MCT simulations [9]. A similar effect is observed in the run length as shown in Figure 3.1. This decrease may be due to the increased local crowding with larger numbers of bound motors. Each motor cannot step until the one in front of it does, which may lead to the reduced velocities we see as the number of motors increases.

We also performed analysis on the factors contributing to the increased processivities in the MCT simulations [9]. In Fig. 3.4, we show that the average number of motors bound to the MT at a given time increases with the number of motors on the cargo. The exponential run length and association time increases may be attributed to this increase in mean bound motors with N_{tot}. While there may be hundreds of motors attached to the cargo at any time, only a handful are within range of the MT and stay consistently bound. Increased numbers of bound motors allow the cargo to be transported much more consistently; if a motor falls unbinds from the MT, there are others that continue to carry the cargo until that motor can stochastically rebind to the MT. This effect leads to increased association time and thus increased run lengths.

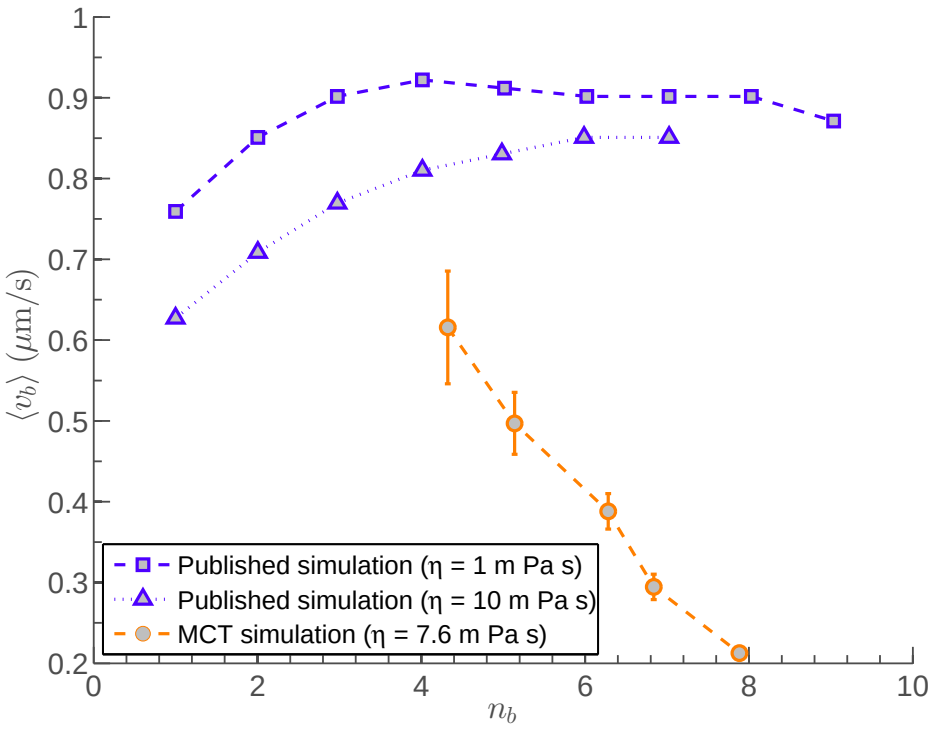

Figure 3.3: Mean run velocity of the cargo as a function of number of motors bound to the MT n_b for different viscosities η. The purple data points show the published data and the orange data points show our MCT implementation [9].

It is important to note that while our MCT simulations results were generally similar to the published MCT model, there were some significant differences in our results. Specifically, the original MCT model featured a nearly constant cargo velocity with N_{tot}, while our version showed a sharp decrease in velocity (shown in Fig 3.3) [9]. This effect is likely caused by a difference in stepping algorithms in the models. The original MCT model ignored the motor's head domain and allowed each motor a binding radius. If this binding radius intersected a predetermined MT binding site, the motor is considered bound to the MT [9]. Conversely, our model calculates the head position of a motor on the cargo explicitly as extending radially outward from the circular cargo. If this motor's head intersects the MT, it is considered bound to the MT at that point.

An important distinction here is that our MCT implementation does not currently have predetermined binding sites, rather motors can bind anywhere and may step only if no other motor is within $\delta = 8\,\text{nm}$. In actuality, MT has distinct binding sites spaced 8 nm apart. It is currently unclear whether our binding site approximation has any significant effects on the simulation.

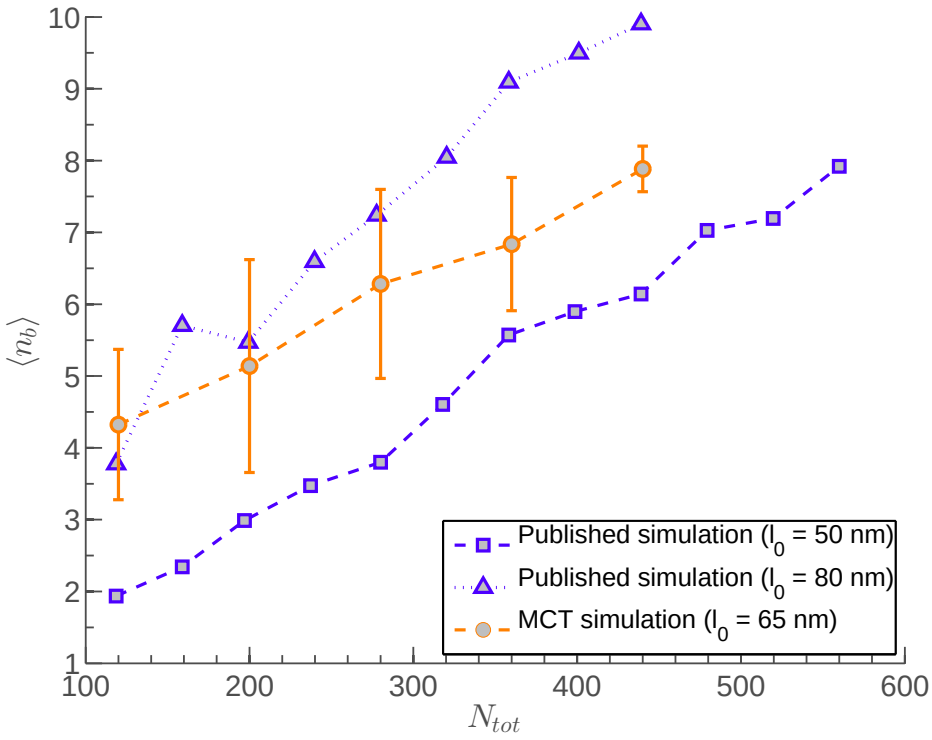

Figure 3.4: Average number of motors bound to the MT as a function of the total motors on the cargo N_{tot}. The purple data points show the published MCT simulation results and the orange data points show our MCT implementation [9].

3.3 Single motor simulation results

The second model we considered was a single motor model, in which a single GFP-labeled kinesin is simulated as it steps along a MT. The parameters for these simulations are given in Table 3.2. A sample kinesin trajectory along the x-axis is shown in Figure 3.5. The single motor steps are calculated at random intervals from its forward stepping rate

$$\lambda_s^0 = \frac{v_0}{\delta} \, . \tag{3.1}$$

Figure 3.6 shows a comparison of our simulation results and the experimental mean run lengths obtained by the Ross lab [4]. Our simulations recapitulate the experimental data reasonably well, as both sets of data feature a distinct change around $\psi \approx 20\,\mathrm{nM}$. It is possible that this is caused by the slowing effects of motor crowding outweighting the motor's unloaded velocity v_0.

Parameter	Typical Value	Meaning	Ref.
R	10 nm	Cargo radius	[4]
T	293 K	Ambient temperature	
η	7.6 mPa s	Viscosity	[4]
h	25 nm	Height from cargo bottom to MT	
$k_{off,0}$	$1/3\,\mathrm{s}^{-1}$	Unstressed escape rate	
ψ	$5, \ldots, 200$ nM Kinesin	Motor Concentration	[4]
ρ	$0\%, \ldots, \mathbf{10}\%, \ldots, 20\%$	Ratio of dead motors	
F_d	2.5 pN	Detachment force	[9]
k	$10^{-5}, \ldots, \mathbf{1.5 \times 10^{-4}}, \ldots, 10^{-3}$ N/m	Kinesin spring constant	[9]
δ	8 nm	Kinesin step size	[6]
v_0	413 nm/s	Maximum motor velocity	
$\lambda_s^0 := v_0/\delta$	$51.6\,\mathrm{s}^{-1}$	Forward stepping rate	
F_s	$\mathbf{5}, \ldots, 8$ pN	Stall force	[6]
l_0	35 nm	Unstressed motor length	
Δt	$1\,\mu$s	Simulation time step	

Table 3.2: Simulation parameters used in the single motor model. If a range is given, the value in bold was the one used in the simulations unless otherwise specified.

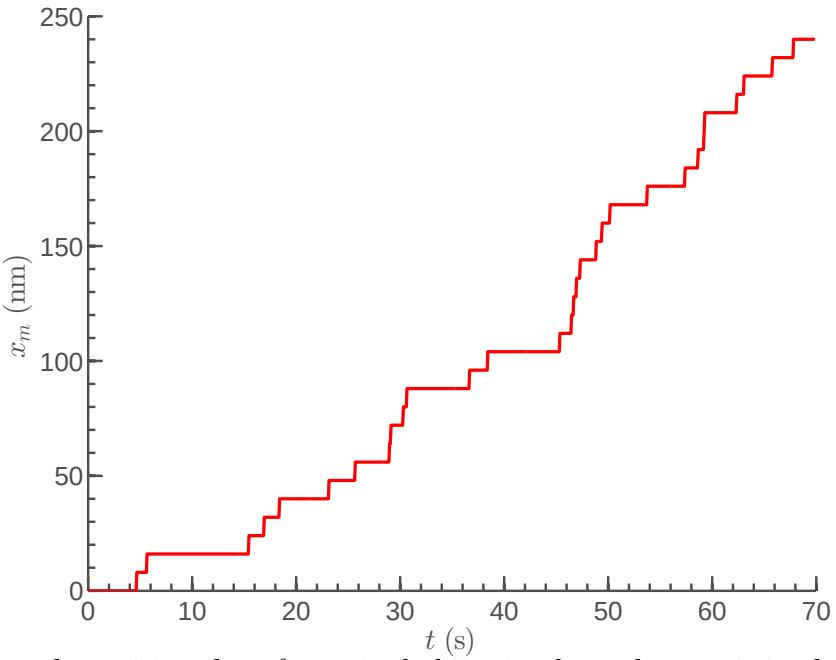

Figure 3.5: Sample position data for a single kinesin along the x-axis in the SM simulations without dead motors. (Parameters: $\psi = 5$ nM, $\rho = 0\%$.)

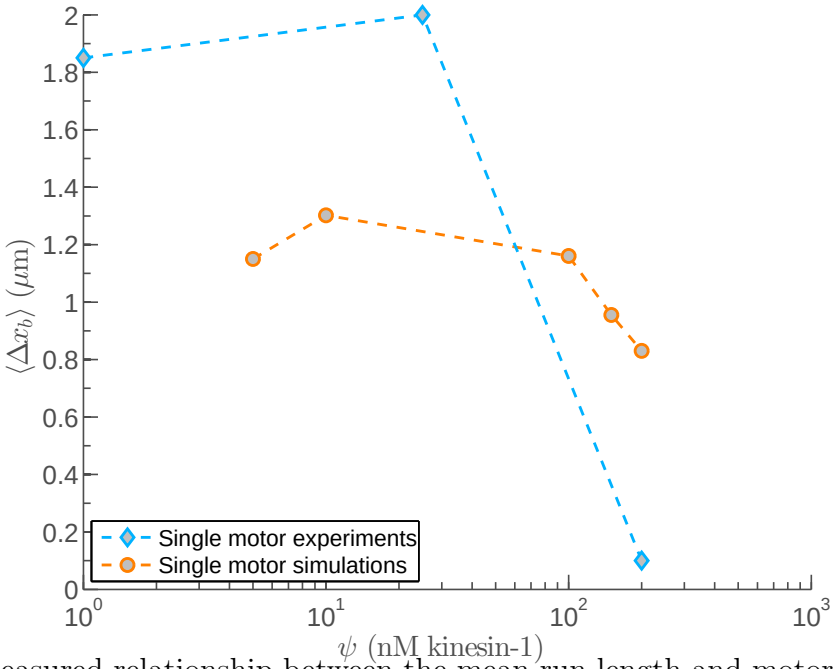

Figure 3.6: Measured relationship between the mean run length and motor concentration ψ for the single motor simulations. The red data points represent our simulation data, while the blue points represent the corresponding single motor experimental data [4].

We can see a similar change in the experimental data, shown in Figure 3.7. The experimental association time appears to be increasing until the value $\psi =$ nM, after which it begins to decline [4]. By contrast, our simulations give a relatively constant association time of 3 seconds, about the same as the expected escape time $k_{off,0} = 1/3\ s^{-1}$.

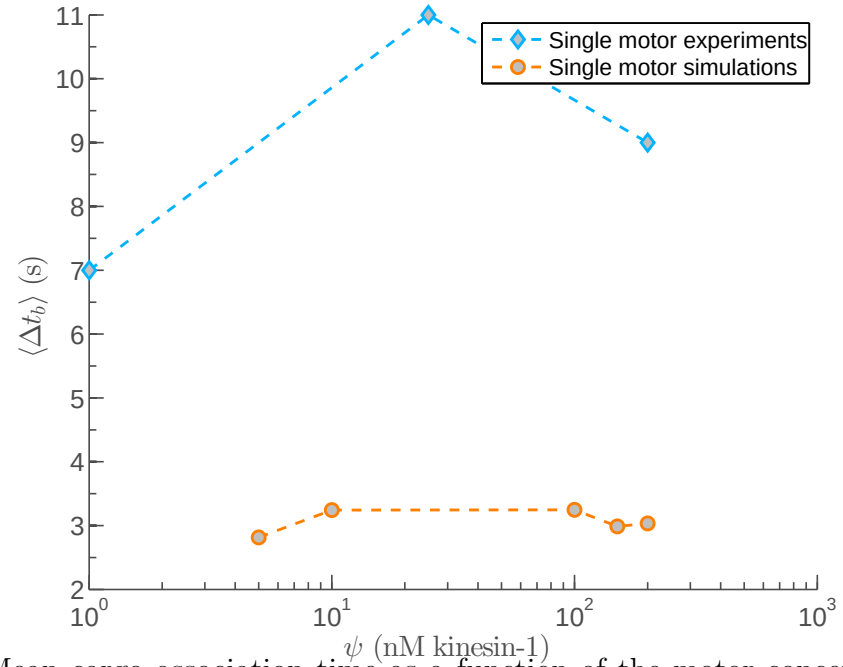

Figure 3.7: Mean cargo association time as a function of the motor concentration ψ. The red data points are our simulation data, while the blue points are the corresponding single motor experimental data [4].

The difference between our simulation and experimental association time has some important implications. We would expect a single kinesin's association time to remain constant as there are presumably no forces acting on it. However, the experimental mean association time experiences an increase and decrease in this value, suggesting that there are additional factors not included in our simple model. We speculate that there may be motor entanglement or other forces introduced at higher motor concentrations. The experimental mean association time also suggest that the unstressed escape rate of the specific kinesin-1 motors may be closer to $k_{off,0} = 1/9\,s^{-1}$, rather than the value $k_{off,0} = 1/3\,s^{-1}$ used in our simulations and in the experiments[4].

The comparison of the GFP-labeled kinesin's mean run velocity for the experimental and simulation data is shown in Figure 3.8. As expected, both data sets show a decrease in velocity as the motor concentration increases [4]. We speculate that this slowing of the single kinesin may be due to increased crowding and pausing due to dead motors. Unfortunately, the experimental data provided to us by our collaborators contained no data on pause frequency or duration for single kinesins.

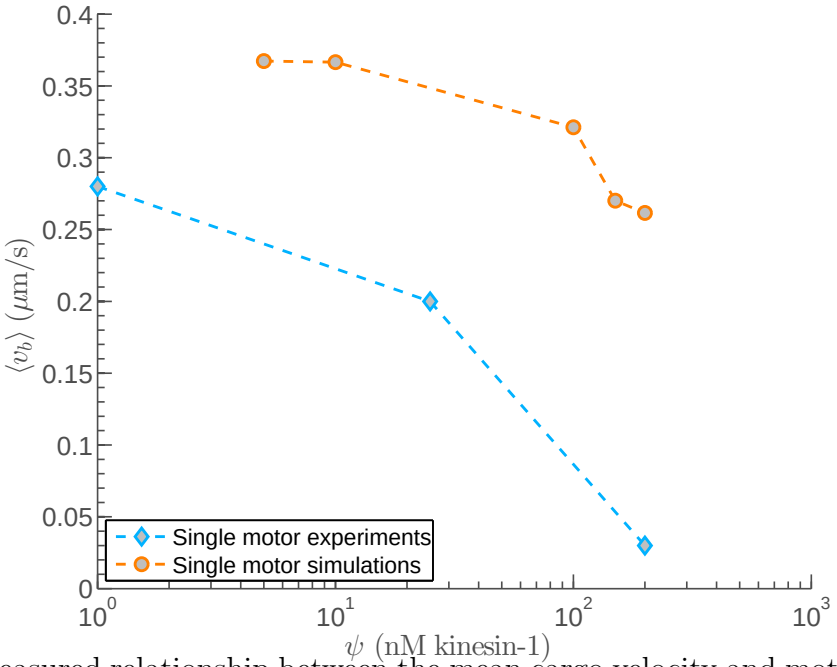

Figure 3.8: Measured relationship between the mean cargo velocity and motor concentration ψ for the single motor simulations. The red data represent our simulation data, while the blue represent the corresponding single motor experimental data [4].

3.4 Improved mechanistic cargo transport simulation results

In Fig. 3.10, we show a example DX visualization from two different motor concentrations in the IMCT simulations. Observe that cargo transport strongly depends on the density of motors nearby, as well as the proximity of any dead motors. This figure shows a visual example of relatively high and low motor densities; the picture on the left has a motor

Parameter	Typical Value	Meaning	Ref.
R	$10\,\text{nm}$	Cargo radius	[4]
T	$293\,\text{K}$	Ambient temperature	
η	$7.6\,\text{mPa s}$	Viscosity	[4]
h	$25\,\text{nm}$	Height from cargo bottom to MT	
$k_{off,0}$	$1/9\,\text{s}^{-1}$	Unstressed escape rate	
ψ	$5, \ldots, 200\,\text{nM}$ Kinesin	Motor Concentration	[4]
ρ	$0\%, \ldots, \mathbf{10}\%, \ldots, 20\%$	Ratio of dead motors	
F_d	$2.5\,\text{pN}$	Detachment force	[9]
k	$10^{-5}, \ldots, \mathbf{1.5 \times 10^{-4}}, \ldots, 10^{-3}\,\text{N/m}$	Kinesin spring constant	[9]
δ	$8\,\text{nm}$	Kinesin step size	[6]
v_0	$413\,\text{nm/s}$	Maximum motor velocity	
$\lambda_s^0 := v_0/\delta$	$51.6\,\text{s}^{-1}$	Forward stepping rate	
F_s	$\mathbf{5}, \ldots, 8\,\text{pN}$	Stall force	[6]
l_0	$35\,\text{nm}$	Unstressed motor length	
Δt	$1\,\mu\text{s}$	Simulation time step	

Table 3.3: Simulation parameters used in the IMCT model. If a range is given, the value in bold was the one used in the simulations unless otherwise specified.

density of $3\,\text{motors}/\mu\text{m}$, while the picture on the right shows a more dense configuration with $30.0\,\text{motors}/\mu\text{m}$.

We can see a sample trajectory of a single motor during cargo transport in Figure 3.9. The motor moves its head domains in discrete stochastic steps, while its tail domain follows the cargo in a fluctuating manner. The source of this random motion experienced by the motor's tail is due to the chaotic Brownian forces experienced by the cargo. As this motor is attached to the cargo, any position or rotation changes experienced by it also affect the motor's tail.

An important result in the IMCT simulations was the role of motor density on other factors like run length, association time and run velocity. Figure 3.11 shows the relationship between motor concentration and run length. We found that increased densities ($\psi \geq 100\,\text{nM}$) led to longer run lengths until a critical value after which a decline is observed. The reason behind this regime change is likely due to the effects of crowding and dead motors at larger densities. Increased numbers of motors mean faster transport and longer association for the cargo, and it would appear that the negative effects of crowding and dead motors outweigh the benefits of increased motor density at the densities $100\,\text{nM}$ or higher in our simulations [4].

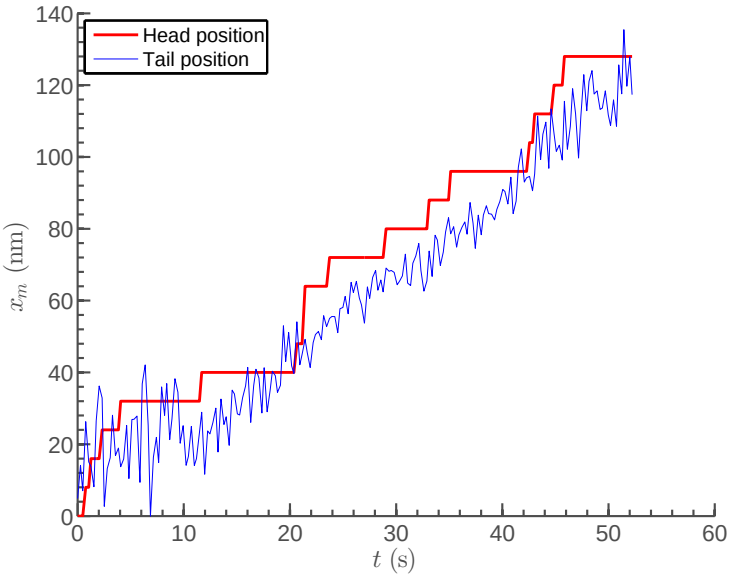

Figure 3.9: Sample position data for a single kinesin during cargo transport in the IMCT simulations without dead motors. The red data points show the motor's head domain position, while the blue data points show the motor's tail domain attached to the cargo. (Parameters: $\psi = 5\,\text{nM}$, $\rho = 0\%$.)

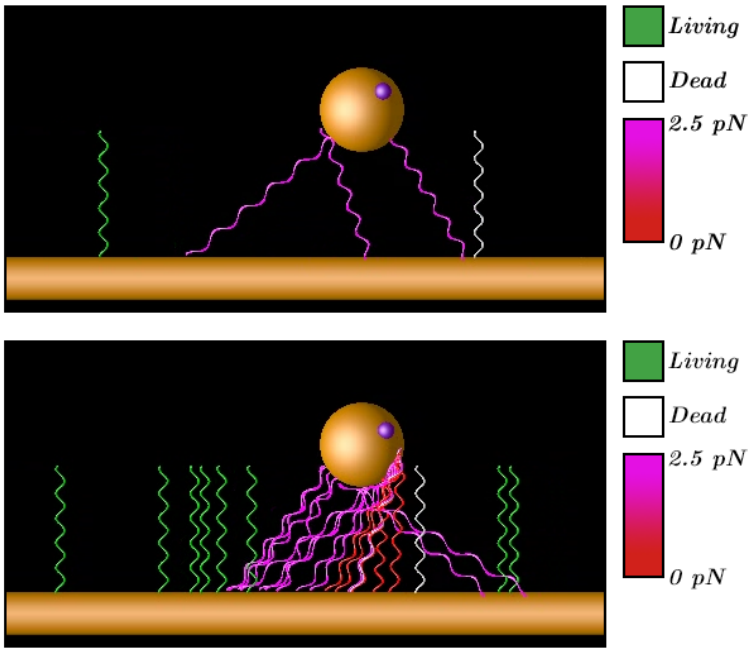

Figure 3.10: Generated video frames from the DX visualization of the IMCT simulations. In (A) we can see a cargo being transported at the relatively low kinesin-1 density of 3.0 motors/μm (B) shows a much higher motor density of 30.0 motors/μm, where increased crowding and traffic jams occur, resulting in distinct movement pauses.

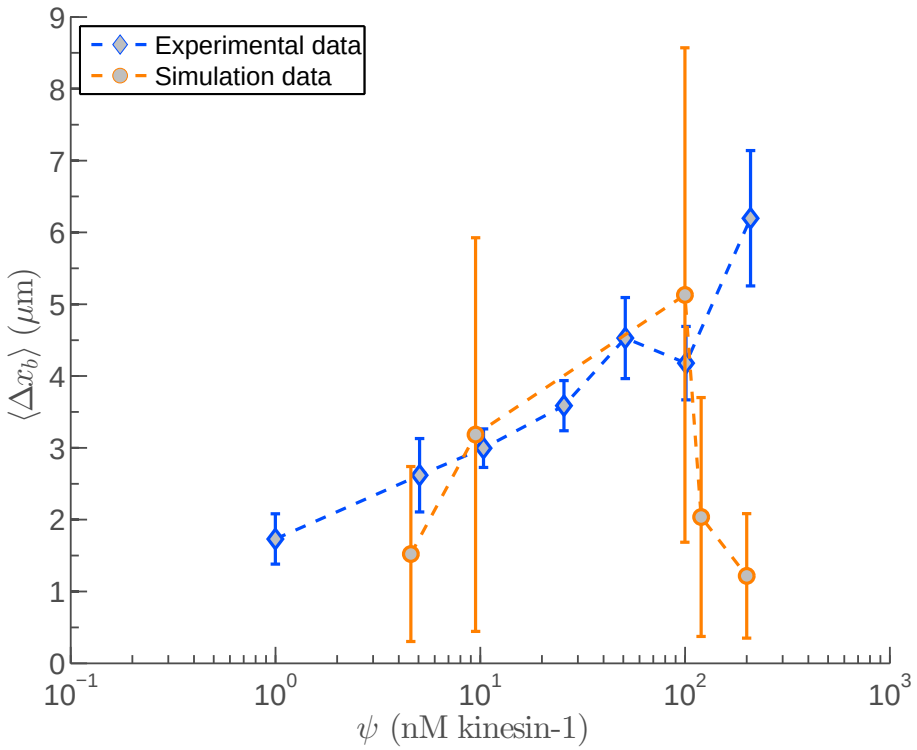

Figure 3.11: Mean cargo run length as a function of motor concentration ψ for the IMCT simulations. The orange data points show the simulation data, while the blue shows the experimental results [4]. (Dead motor percentage, $\rho = 10\%$.)

We preformed a similar analysis on the effects of motor density on association time. Figure 3.12 shows effects similar to those previously described in Figure 3.11: a distinct regime change above the motor density $\psi = 100\,\text{nM}$. Although the error bars in the figure are relatively large, they do show an increase in velocity up until this point, when it begins to decline or perhaps remain constant. We expect that this is due to the increased processivity of the cargo being outweighted by the additional forces introduced by the dead motor-induced pausing [4].

We repeated the motor density dependence analysis with the quantum-dot's average velocity. Average velocity values were recorded during short time intervals (70 ms) and later divided into two parts: with and without pauses included. Note that the velocity decreases consistantly as the motor density increases. This result is expected, as increased motor concentration ψ leads to increased pausing due to dead motors and increased crowding. We note that even with cargo pauses excluded from our analysis, the cargo velocity still decreases with the motor concentration. This effect may be attributed to the increased motor crowding, meaning that more motors cannot step because they are waiting for the binding site in front of them to be cleared, thus a decrease in cargo transport velocity [4].

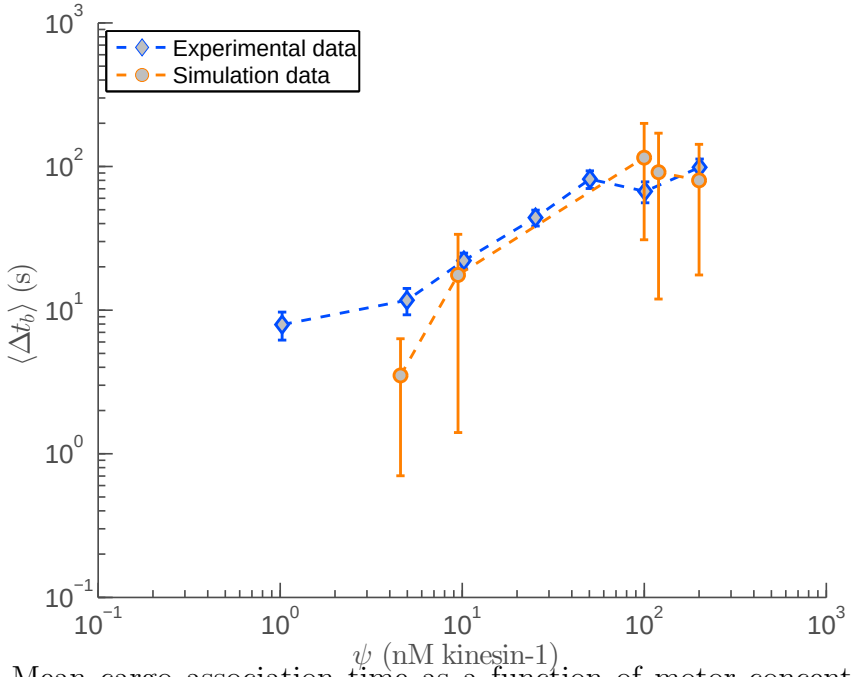

Figure 3.12: Mean cargo association time as a function of motor concentration ψ for the IMCT simulations. The orange data points show the simulation data, while the blue points show the experimental results [4]. (Dead motor percentage, $\rho = 10\%$.)

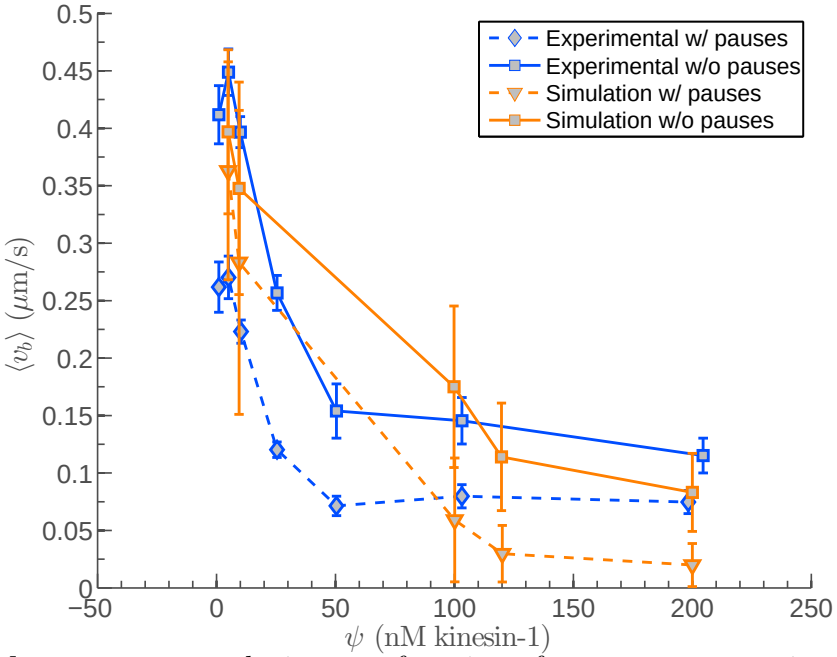

Figure 3.13: Mean cargo run velocity as a function of motor concentration ψ for the IMCT simulations. The orange data points show the simulation data with (solid line) and without pauses (dotted line,) while the blue points show the experimental results with (solid line) and without pauses (dotted line) [4]. (Dead motor percentage, $\rho = 10\%$.)

Taking into account the distinct decreases in run length and association time observed at $\psi \geq 100\,\text{nM}$ and the decreasing cargo velocities throughout, Figures 3.14 and 3.15 shows the

expected increase in pauses as motor density increases. These figures effectively normalize the number of pauses over a run's association time and run length. Both plots show that the frequency of pausing generally increases as the motor density increases [4].

In Figure 3.16, we can see an increase in bound motor numbers at higher motor densities. These larger numbers of bound motors lead to longer association times and increased load sharing between motors [4]. As mentioned previously, more motors bound to the cargo means more crowding, which can reduce the cargo's mean velocity. One effect observed from our OpenDX visualizations was that cargos tend to gather extra motors during their pauses. Because the cargo cannot move, motors behind it walk directly into the cargo, becoming bound to it in the process.

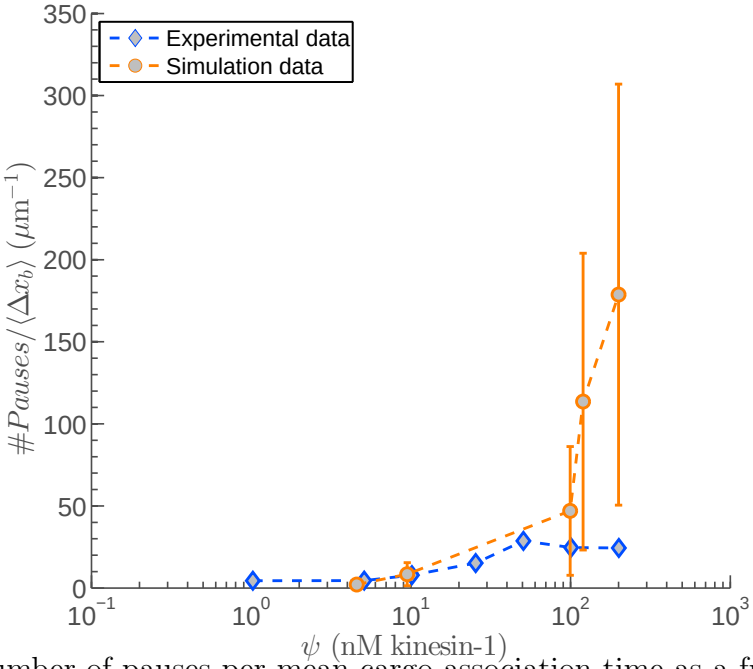

Figure 3.14: The number of pauses per mean cargo association time as a function of motor concentration ψ for the IMCT simulations. The orange data points show the simulation data while the red data points show the experimental results [4]. (Dead motor percentage, $\rho = 10\%$.)

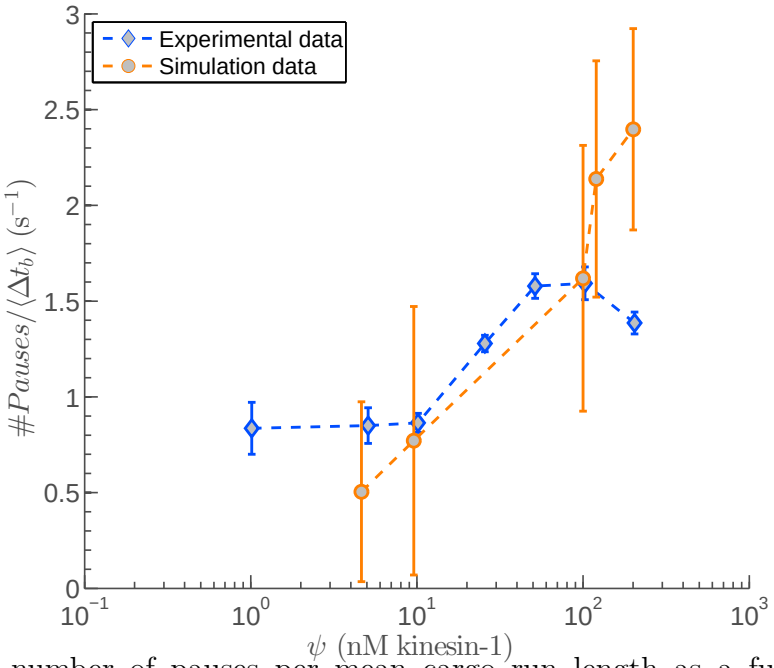

Figure 3.15: The number of pauses per mean cargo run length as a function of motor concentration ψ for the IMCT simulations. The orange data points show the simulation data while the red data points show the experimental results [4]. (Dead motor percentage, $\rho = 10\%$.)

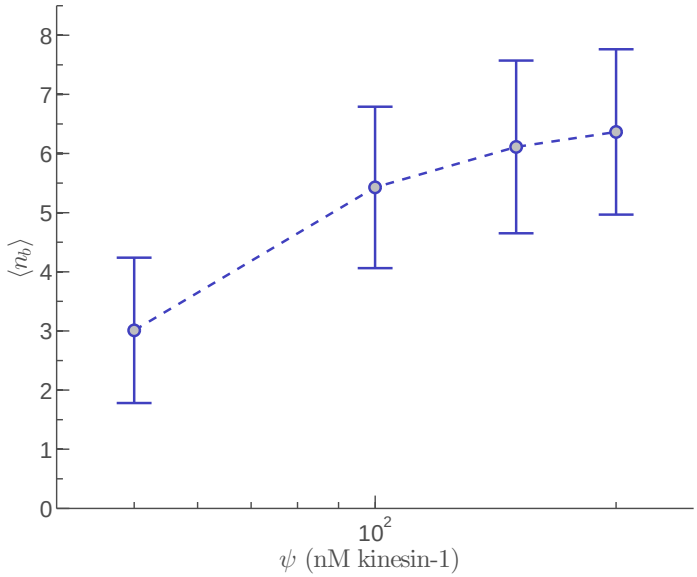

Figure 3.16: Mean number of cargo-bound kinesins as a function of motor concentration ψ. (Dead motor percentage, $\rho = 10\%$.)

Figure 3.17 shows the relationship between percentage of time spend paused and motor density. This graph further supports the concept of a change at $\psi \geq 100\,\text{nM}$, as there is a reduction in time in this range. Again, this result is expected as increased motor concentrations lead to increased crowding and dead motors, which are the main source of

pausing during cargo transport in our simulations.

Overall, we found that our models match the corresponding published data sets reasonably well. In the MCT and IMCT models, we found a few disputes in our results, specifically the distinct velocity decreases with ψ. The single motor published data differs notably from our single motor model for run length and association time. A non linear experimental association time seems to suggest that there may be additional forces occuring during cargo transport that are not captured in the current models.

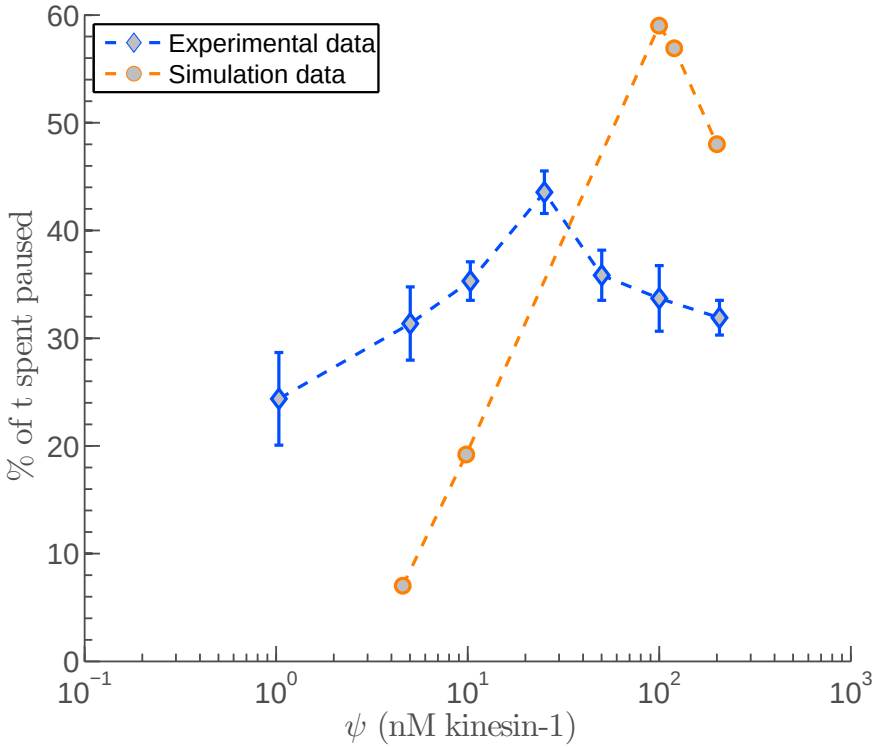

Figure 3.17: Average percent of cargo association time spend paused for different values of motor concentration ψ. The orange data points represents the simulation results, while the red data points represent the analogous experimental data [4]. (Dead motor percentage, $\rho = 10\%$.)

3.4.1 Analysis of forces

In order to understand some of the complex motor-cargo interactions that occur during cargo transport, we did a brief analysis of the forces involved. Figures 3.18, 3.19 and 3.20 show the distribution of motor forces during cargo transport without dead motors present for different motor concentrations. These histograms are relatively symmetrical, and do not seem to vary much between motor densities. The charts show that during cargo transport, the cargo experiences motors pulling both from the front and from the back. Note that this distribution of forces may be quite different if the cargo did not experience Brownian motion, as this is one of the prominant causes of kinesin stretching.

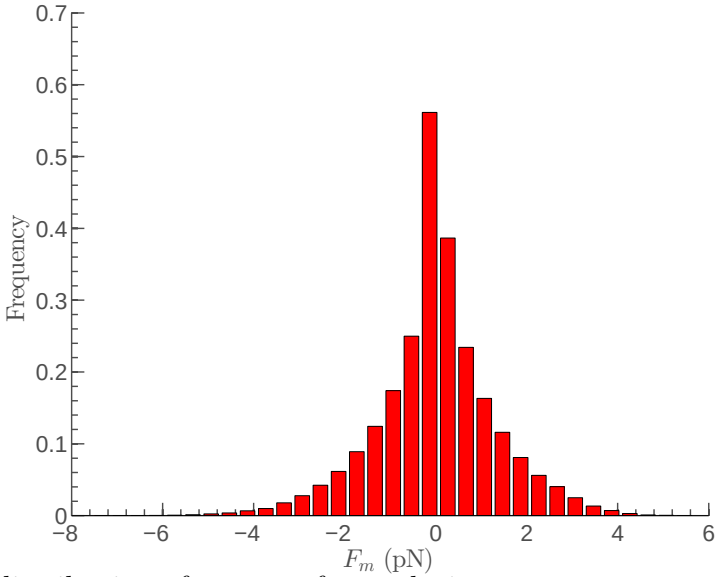

Figure 3.18: The distribution of motor x-forces during cargo transport with a motor concentration of $\psi = 5\,\text{nM}$ in the IMCT simulations. (Dead motor percentage, $\rho = 0\%$.)

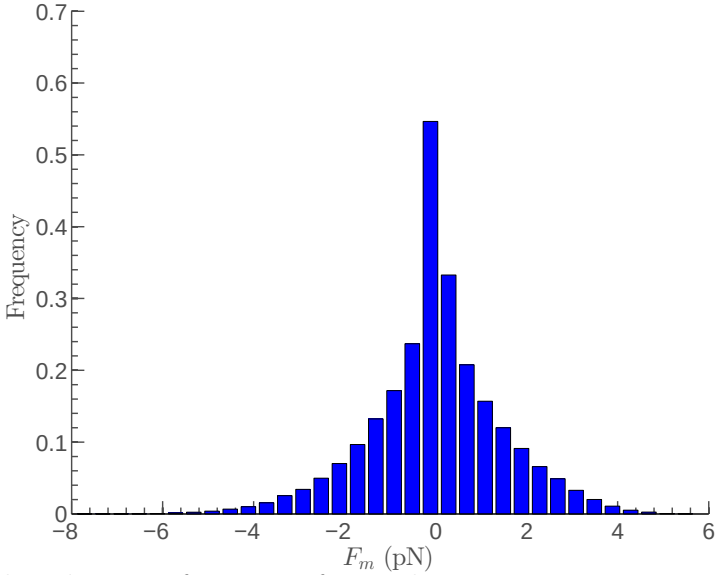

Figure 3.19: The distribution of motor x-forces during cargo transport with a motor concentration of $\psi = 100\,\text{nM}$ in the IMCT simulations. (Dead motor percentage, $\rho = 0\%$.)

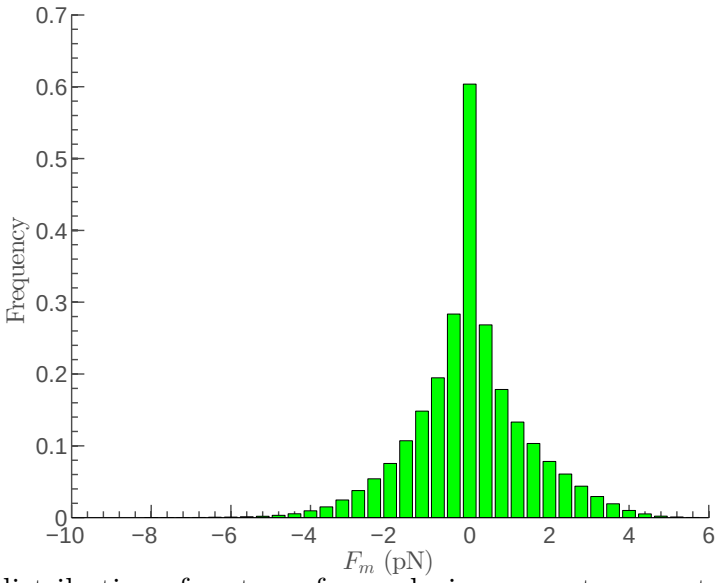

Figure 3.20: The distribution of motor x-forces during cargo transport with a motor concentration of $\psi = 200\,\text{nM}$ in the IMCT simulations. (Dead motor percentage, $\rho = 0\%$.)

We also analyzed the average motor detachment forces during transport, in Figures 3.21, 3.22 and 3.23. It is important to note that the detachment force $F_d = 2.5$ pN in these simulations. As expected, most of the detachment forces appear to be below this value. Forces larger than 2.5 pN can be explained by the cargo's Brownian motion, causing large position jumps which then can cause large motor stretching that occurs briefly before the motor is dissociated. Although Fig. 3.21 ($\psi = 10$ nM) is noisier than the others, all three figures appear to follow the same trends.

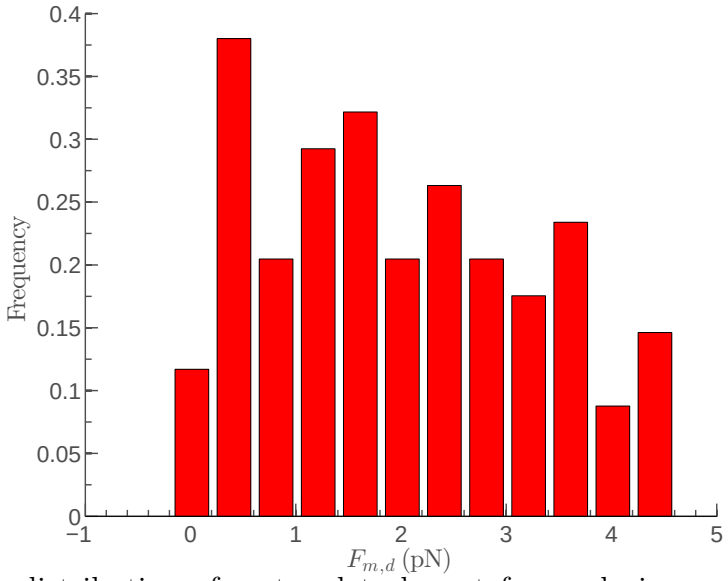

Figure 3.21: The distribution of motor detachment forces during cargo transport with a motor concentration of $\psi = 5\,\text{nM}$ in the IMCT simulations. (Dead motor percentage, $\rho = 0\%$.)

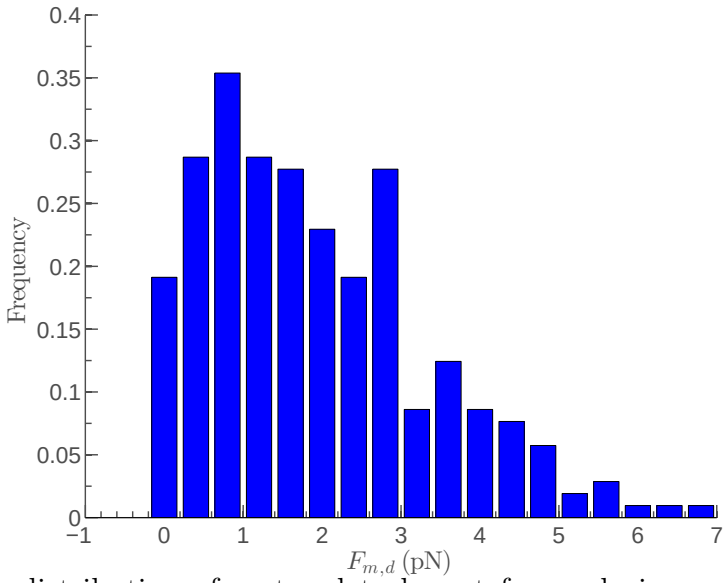

Figure 3.22: The distribution of motor detachment forces during cargo transport with a motor concentration of $\psi = 100\,\text{nM}$ in the IMCT simulations. (Dead motor percentage, $\rho = 0\%$.)

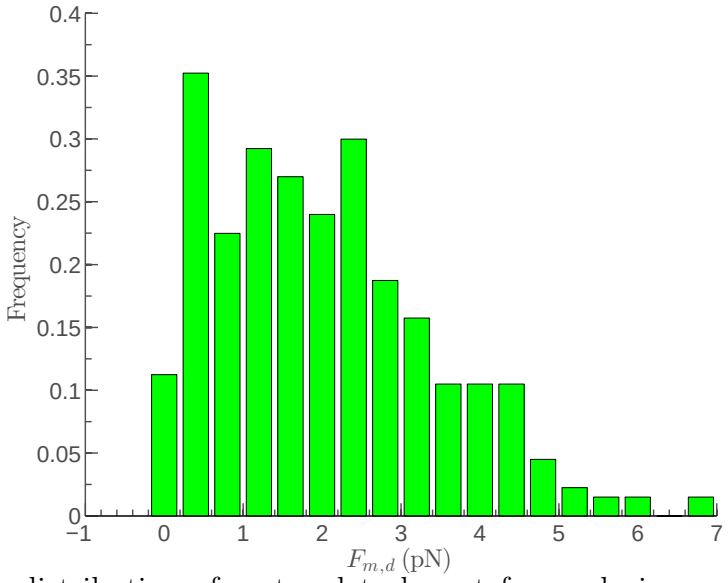

Figure 3.23: The distribution of motor detachment forces during cargo transport with a motor concentration of $\psi = 200\,\text{nM}$ in the IMCT simulations. (Dead motor percentage, $\rho = 0\%$.)

We observe similar behavior in Figures 3.24, 3.25 and 3.26, which show the distribution of motor detachment lengths during cargo transport. The shape of the histograms appears to match the corresponding detachment force histograms. Note that the most common detachment lengths are relatively close to the unstressed motor length $l_0 = 35$ nm. These plots also demonstrate the pseudo-spring modelling of kinesins in our simulations; most of the motors experience detachment with lenghts $l > l_0$. The few motors that are compressed exert no forces on the cargo.

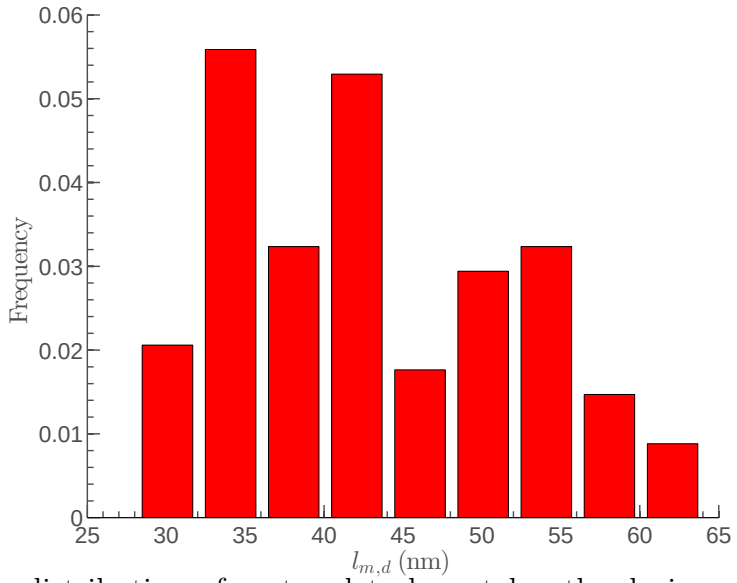

Figure 3.24: The distribution of motor detachment lengths during cargo transport with a motor concentration of $\psi = 5\,\text{nM}$ in the IMCT simulations. (Dead motor percentage, $\rho = 0\%$.)

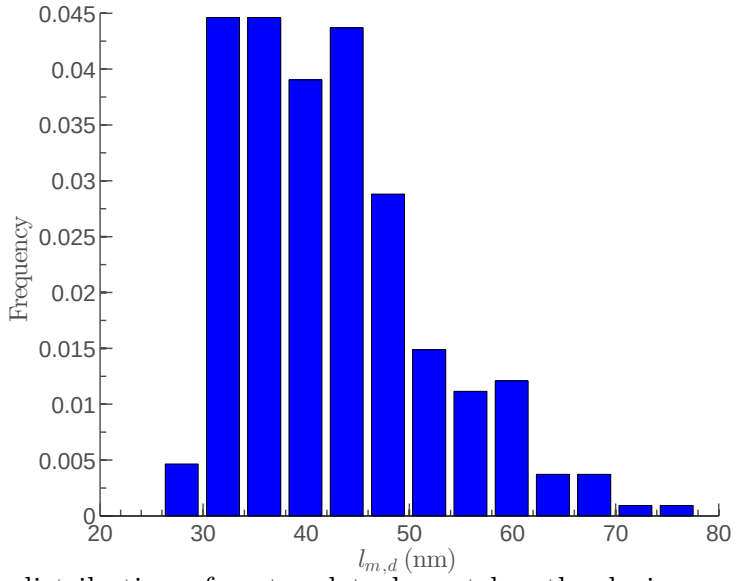

Figure 3.25: The distribution of motor detachment lengths during cargo transport with a motor concentration of $\psi = 100\,\text{nM}$ in the IMCT simulations. (Dead motor percentage, $\rho = 0\%$.)

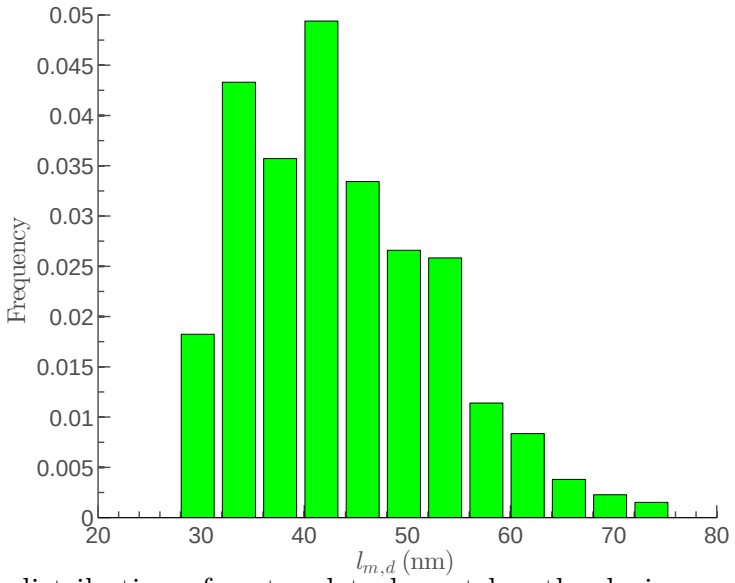

Figure 3.26: The distribution of motor detachment lengths during cargo transport with a motor concentration of $\psi = 200\,\text{nM}$ in the IMCT simulations. (Dead motor percentage, $\rho = 0\%$.)

Chapter 4

Conclusions and Future Directions

We developed a coarse-grained two-dimensional stochastic model of cargo transport via kinesin-1 motor proteins and compared it with experimental results at high motor concentrations. This technique eventually branched into three distinct models: Mechanistic Cargo Transport, single motor and Improved Mechanistic Cargo Transport. We found that our improved model recapitulated the available experimental results relatively well.

In the future, we hope to expand this model to include additional mechanics that might occur during cargo transport. One feature we have been investigating is the existence of multiple protofilaments. Motors from diferent tracks may be able to bind to and carry cargo simultaneously, which will have effects on processivity and pauses during transport. Additionally, some of the single motor experimental results suggest that there may be additional forces felt by individual motors at higher motor concentrations. These forces could be introduced by some sort of motor entanglement.

We also hope to extend our model to include additional cargo types. In its current form, the mechanistic model only includes circular cargos, but we hope to implement other cargo shapes into the model. It would also be possible to extend this model to include other processive motors in the kinesin family. This feature would allow us to simulate cargo transport with different types of motors at the same time, each with its own stepping rate, compliance, stalk length, etc.

Bibliography

[1] OpenDX, 2013. URL `http://www.opendx.org`. Accessed: 03/04/2013.

[2] Howard C. Berg and Freeman Dyson. Random walks in biology. *Physics Today*, 40(3): 73–74, 1987.

[3] Jared C. Cochran, Christopher A. Sontag, Zoltan Maliga, Tarun M. Kapoor, John J. Correia, and Susan P. Gilbert. Mechanistic analysis of the mitotic kinesin eg5. *Journal of Biological Chemistry*, 279(37):38861–38870, 2004.

[4] Leslie Conway, Derek Wood, Erkan Tüzel, and Jennifer L. Ross. Motor transport of self-assembled cargos in crowded environments. *Proceedings of the National Academy of Sciences*, 109(51):20814–20819, 2012.

[5] William O. Hancock and Jonathon Howard. Processivity of the motor protein kinesin requires two heads. *The Journal of Cell Biology*, 140:1395–1405, 1998.

[6] J Howard. The movement of kinesin along microtubules. *Annual Review of Physiology*, 58:703–729, 1996. ISSN 0066-4278.

[7] Stefan Klumpp and Reinhard Lipowsky. Cooperative cargo transport by several molecular motors. *Proceedings of the National Academy of Sciences of the United States of America*, 102:17284–17289, 2005.

[8] Donald Knuth. *Fortran Numerical Recipes, Second Edition*, volume 2. Cambridge University Press, 1992.

[9] Christian B. Korn, Stefan Klumpp, Reinhard Lipowsky, and Ulrich S. Schwarz. Stochastic simulations of cargo transport by processive molecular motors. *The Journal of Chemical Physics*, 131, 2009.

[10] C. Leduc, K. Padberg-Gehle, V. Varga, D. Helbing, S. Diez, and J. Howard. Molecular crowding creates traffic jams of kinesin motors on microtubules. *Proceedings of the National Academy of Sciences of the United States of America*, 109:1600–1605, 2012.

[11] Marcy E. MacDonald, Silvia Gines, James F. Gusella, and Vanessa C. Wheeler. Huntington's disease. *NeuroMolecular Medicine*, 4:7–20, 2003. ISSN 1535-1084.

[12] Karen McNally, Anjon Audhya, Karen Oegema, and Francis J. McNally. Katanin controls mitotic and meiotic spindle length. *The Journal of Cell Biology*, 175(6):881–891, 2006.

[13] Andrew H. Nguyen, Erkan Tüzel, and Benjamin L. Stottrup. Lipid monolayer line tension measurements and model convolution. *Biophysical Journal*, 98(3, Supplement 1):275a –, 2010. ISSN 0006-3495.

[14] Encyclopædia Britannica Online. Cell (biology), 2013. URL `http://www.britannica.com.ezproxy.wpi.edu/EBchecked/topic/380723/microtubule`. [Online; accessed 24-February-2013].

[15] Encyclopædia Britannica Online. Bacteria, 2013. URL `http://www.britannica.com/EBchecked/topic/48203/bacteria/39334/Diversity-of-structure-of-bacteria`. [Online; accessed 24-February-2013].

[16] Mariana Ruiz, 2006. URL `http://commons.wikimedia.org/wiki/File:Animal_cell_structure_en.svg`.

[17] Mark J. Schnitzer, Koen Visscher, and Steven M. Block. Force production by single kinesin motors. *Nature Cell Biology*, 2:718–723, 2000.

[18] Slagt, 2006. URL `http://commons.wikimedia.org/wiki/File:Motility_of_kinesin.png`.

[19] Vladimir Varga, Cecile Leduc, Volker Bormuth, Stefan Diez, and Jonathon Howard. Kinesin-8 motors act cooperatively to mediate length-dependent microtubule depolymerization. *Cell*, 138(6):1174 – 1183, 2009. ISSN 0092-8674.

[20] Zlir'a, 2011. URL `http://commons.wikimedia.org/wiki/File:Microtubule_id.svg`.